1 The strain-dependent spatial evolution of garnet in
2 a high-pressure ductile shear zone from the
3 Western Gneiss Region (Norway): a Synchrotron
4 x-ray microtomography study

5 Alice Macente (Corresponding author)
6 School of Geosciences, The King's Building, James Hutton Road, Edinburgh, EH9 3FE
7 Email: alice.macente@ed.ac.uk

8 Florian Fusseis, School of Geosciences, The King's Building, James Hutton Road,
9 Edinburgh, EH9 3FE

10 Luca Menegon, School of Geography, Earth and Environmental Sciences (Faculty of
11 Science and Engineering), Fitzroy, Drake Circus, Plymouth, Devon, PL4 8AA

12 Xianghui Xiao, Argonne National Laboratory, 9700 S. Cass Ave, Building 431-B003

13 Timm John, Institut für Geologische Wissenschaften, Freie Universität Berlin,
14 Malteserstr. 74-100, 12249 Berlin
15

16 **Short title:** Strain-dependent evolution of garnet
17

1

18   **Abstract**

19   Reaction and deformation microfabrics provide key information to understand the

20   thermodynamic and kinetic controls of tectono-metamorphic processes, however they are

21   usually analysed in two dimensions, omitting important information regarding the third

22   spatial dimension. We applied Synchroton-based x-ray microtomography to document

23   the evolution of a pristine olivine gabbro into a deformed omphacite-garnet eclogite in

24   four dimensions, where the 4th dimension is represented by the degree of strain. In the

25   investigated samples, which cover a strain gradient into a shear zone from the Western

26   Gneiss Region (Norway), we focused on the spatial transformation of garnet coronas into

27   elongated clusters of garnets with increasing strain. Our microtomographic data allowed

28   quantification of garnet volume, shape and spatial arrangement evolution with increasing

29   strain. We combined microtomographic observations with light microscope- and

30   backscatter electron images as well as electron microprobe- (EMPA) and electron

31   backscatter diffraction (EBSD) analysis to correlate mineral composition and orientation

32   data with the x-ray absorption signal of the same mineral grains.

33   With increasing deformation, the garnet volume almost triples. In the low strain domain,

34   garnets form a well interconnected large garnet aggregate that develops throughout the

35   entire sample. We also observed that garnet coronas in the gabbros never completely

36   encapsulate olivine grains. In the most highly deformed eclogites, the oblate shapes of

37   garnets reflect a deformational origin of the microfabrics. We interpret the aligned garnet

38   aggregates to direct synkinematic fluid flow and consequently influence the transport of

39   dissolved chemical components. EBSD analyses reveal that garnet show a near-random

40   crystal preferred orientation that testifies no evidence for crystal plasticity. There is,

2

41   however evidence for minor fracturing, neo-nucleation and overgrowth. Microprobe

42   chemical analysis revealed that garnet compositions progressively equilibrate to eclogite

43   facies, becoming more almandine-rich. We interpret these observations as pointing to a

44   mechanical disintegration of the garnet coronas during strain localisation, and their

45   rearrangement into individual garnet clusters through a combination of garnet

46   coalescence and overgrowth while the rock was deforming.

47

48   **Key words:**

49   Synchrotron x-ray microtomography; garnet; high-pressure shear zone; Western Gneiss

50   Region; strain localisation;

51

52 **INTRODUCTION**

53 Synkinematic reaction microfabrics carry important information on the kinetics, timing,

54 and mechanics of tectono-metamorphic processes. The spatial arrangement of reaction

55 products reflects directions and magnitudes of mass and element transport. An

56 assessment of the geometry of reaction microfabrics is therefore a critical component in

57 reconstructing the tectono-metamorphic evolution of a rock. Despite being routinely

58 interpreted in metamorphic and structural studies, reaction and deformation

59 microfabrics are usually described in two dimensions, which can lead to incorrect

60 petrographic and structural interpretations. In this study, we use garnet to explore the

61 significance of a 3-dimensional (3D) approach to the description of synkinematic

62 reactions and deformation microfabrics.

63 In nature, garnet represents an extremely versatile recorder of metamorphism (Baxter &

64 Scherer, 2013) and in particular garnet coronas capture metamorphic processes "in

65 flagranti" (Carlson & Johnson, 1991; Carlson, 2011; Ague & Carlson, 2013).

66 Consequently, garnet coronas and their metamorphic significance have been intensely

67 studied over the past decades (Mørk, 1985; Johnson & Carlson, 1990; Johnson, 1993;

68 Spiess *et al.*, 2001; Prior *et al.*, 2002; Konrad-Schmolke *et al.*, 2005; Massey *et al.*,

69 2011; Goergen & Whitney, 2012).

70 Garnet porphyroblasts often hold the key to unravel the synkinematic PTtd conditions.

71 The origin of these garnet porphyroblasts has been controversially discussed as either

72 being evidence of rotational strains (*"Snowball garnets"*, Johnson, 1993; Jiang &

73 Williams, 2004), as documenting strain partitioning (Bell & Johnson, 1989; Aerden,

74 2005) or, where polycrystalline, as forming from the coalescence of nuclei (Spiess *et*

75   *al*., 2001, Dobbs *et al.* 2003).

76   Garnet also readily partakes in mylonitic deformation: crystal plastic deformation of

77   garnets at lower crustal conditions was documented by, e.g., Ji & Martignole (1994), Ji

78   & Martignole (1996), Prior *et al.*, (2002), Storey & Prior (2005), Massey, Prior &

79   Moecher (2011), Martelat *et al.*, (2012). Garnets in mylonitic eclogites from SW

80   Norway were shown to have deformed by grain-boundary diffusion creep and by

81   pressure-solution (Smit *et al.*, 2011). However, garnet in eclogitic mylonitized

82   micaschits was also shown to have deformed by cataclasis and frictional sliding

83   (Trepmann & Stöckhert, 2002).

84   Conclusions derived in these studies often invoke an extrapolation from the second to

85   the third spatial dimension, which is naturally speculative. With the advent of x-ray

86   microtomography, garnet became the focus of a number of microstructural studies that

87   explored the third spatial dimension (Denison & Carlson, 1997; Ketcham, 2005a;

88   Whitney *et al.*, 2008; Goergen & Whitney, 2012).

89   These pioneering 3-dimensional studies outlined the possibilities that the combination of

90   x-ray microtomographic data with other microanalytical techniques holds in regards to

91   the interrogation of tectono-metamorphic processes. In this present contribution, we

92   apply this approach to analyse the distribution of garnet in rock samples from

93   Kråkeneset, a tectonic domain within the well-studied Western Gneiss Region (Norway)

94   (Mørk, 1985; Mørk, 1986; Austrheim, 1987; Boundy *et al.*, 1992; Austrheim *et al.*, 1997;

95   Krabbendam &Dewey, 1998; Cuthbert *et al.*, 2000; Engvik *et al.*, 2000; Krabbendam *et*

96   *al.*, 2000; Engvik *et al.*, 2001; Wain *et al.*, 2001; Labrousse *et al.*, 2004; Terry &

97   Heidelbach, 2006; John *et al.*, 2009; Hacker & Andersen, 2010; Labrousse *et al.*, 2010).

5

98   There, fluid infiltration along precursory fractures led to the eclogitization and coeval

99   mylonitic overprint of gabbroic rocks (Mørk, 1985; Austrheim *et al.*, 1997; Krabbendam

100   *et al.*, 2000; Engvik *et al.*, 2001; Lund & Austrheim, 2003; John *et al.*, 2009; Müller,

101   2013). Our field location is a gabbroic body in which hydrous eclogite-facies shear

102   zones cross cut the almost pristine magmatic rock. There, reaction textures indicate that

103   the eclogite-facies overprint is caused by the ingress of reactive fluids that helped to

104   overcome sluggish reaction kinetics (Austrheim, 1987; Krabbendam *et al.*, 2000; Lund &

105   Austrheim, 2003; John *et al.*, 2009; Müller, 2013). The rock samples cover a strain

106   gradient (which we consider the 4th dimension) into a dm-scale mylonitic shear zone and

107   document the metamorphic overprint. The strain gradient along the shear zones is ideally

108   suited for such a study, in that it shows progressive deformation localization under well

109   constrained P-T-fluids conditions. Based on the assumption that the strain gradient can

110   be regarded as a proxy for time, which is a common assumption where strain softening

111   leads to progressive strain localisation (Means, 1995; Fusseis, *et al.*, 2006; Fusseis &

112   Handy, 2008), the samples allow us to characterize the spatiotemporal evolution of a

113   gabbro into a deformed eclogite. In our samples, this transition is reflected by the

114   evolving 3-dimensional distribution of garnets in the microfabric. We determine how the

115   garnet evolved from its arrangement in a primary coronitic texture to forming a key

116   component of the tectonic microfabric. To do this, we developed a methodological

117   workflow that combined classical electron-beam techniques with Synchroton x-ray

118   microtomography. In combination, these data allow us to speculate on the mechanisms

119   that accomplished the transformation of garnet microfabrics.

120   **GEOLOGICAL SETTING**

6

121   The studied rock samples come from Kråkeneset in the Western Gneiss Region (WGR)

122   of the Norwegian Caledonides. As many other parts of this lowest tectonic unit in the

123   Scandinavian terrains, the outcrops in Kråkeneset preserve evidence for Caledonian high-

124   pressure metamorphism in association with the subduction of Baltica underneath

125   Laurentia after the Silurian closure of the Iapetus ocean (Engvik, *et al.,* 2000;

126   Krabbendam *et al.*, 2000; Wain *et al.,* 2001; Lund & Austrheim, 2003; Labrousse *et al.*,

127   2004; John *et al.*, 2009; Müller, 2013). It is commonly accepted that even though some

128   of the rocks in the WGR were subducted to depths beyond 100 km, large parts of the

129   complex remained metastable until fluid infiltration along brittle fractures and cleavage

130   planes overcame sluggish reaction kinetics and initiated large-scale eclogitisation

131   (Austrheim, 1987; Krabbendam *et al.*, 2000; Wain *et al.*, 2001; Labrousse *et al.*, 2010).

132   In Kråkeneset, the high-pressure metamorphic overprint takes the form of hydrous

133   eclogites that occur within shear zones cutting dry grabbroic host rocks (Krabbendam, *et*

134   *al.*, 2000; Lund & Austrheim, 2003; John *et al.*, 2009). The pristine gabbroic mineral

135   assemblage is preserved in the less deformed areas, and is characterized by an ophitic

136   texture, in which garnet and orthopyroxene coronas surround olivine cores. Previous

137   authors have interpreted these coronas as having derived from diffusion-controlled

138   reactions of olivine and plagioclase (Mørk, 1985; Johnson & Carlson, 1990). The

139   eclogite-facies mineral assemblages occur within narrow shear zones where, across their

140   margin, a gradient from a "dry" gabbroic mineral assemblage (Ol + Cpx + Grt + Pl + Ilm

141   + Bt + Am ± Rt), to a synkinematic mostly "wet" eclogitic mineral assemblage is

142   preserved. The latter consists of Grt + Opx + Am + Ab-Czo symplectites + Bt + Opaque

143   phases (e. g Ilm) ± phengite, as well as omphacite + garnet (Fig. 4), where the reaction

7

144 advanced further or local chemical domains supported this assemblage (Austrheim, 1987;

145 Lund & Austrheim, 2003; John *et al.*, 2009; Putnis & Austrheim, 2010; Müller, 2013).

146 The replacement of magmatic plagioclase by Ab-Czo symplectites (e.g., Wayte et al.,

147 1989), along with the widespread formation of amphiboles and of Grt-Omp assemblages,

148 occurs where transport during reactions has been enhanced (e.g., Mørk, 1985; John &

149 Schenk, 2003; Putnis & Austrheim, 2010). All these developments positively correlate

150 with the observed strain gradient, and show that eclogitization of the gabbro was driven

151 by the close interplay of infiltration of externally derived fluids and deformation (Mørk,

152 1985; Austrheim, 1987; Krabbendam *et al.*, 2000; Lund & Austrheim, 2003; Labrousse

153 *et al.*, 2010; Putnis & John, 2010).

154 **METHODS**

155 From a hand specimen that covers the margin of an eclogite shear zone, three 2-mm

156 thick rock wafers covering the strain gradient were extracted in x-z kinematic

157 orientations (Fig. 1). From these wafers, parallelepipeds with dimensions of 2x2x6 mm

158 were cut for Synchrotron x-ray microtomography (SµCT). After SµCT, the wafers

159 including the SµCT samples were polished into thin sections that could be used for

160 further analyses using light microscopy, scanning electron microscopy (SEM), electron

161 microprobe analyses (EMPA) and electron backscatter diffraction (EBSD). This

162 approach allowed for a comprehensive characterisation of the metamorphic

163 microfabrics in four dimensions (Fig. 1). This study focussed on three specimens,

164 #066B2, #061751 and #0618, which sample the low-, intermediate- and high-strain

165 domain of the shear zone.

166 **Analytical Techniques**

8

167 Mineral assemblage and chemical zoning were analysed on the carbon-coated thin

168 sections using a Zeiss SIGMA HD VP Field Emission SEM equipped with an Oxford

169 Instruments SD EDS detector and AZtec software for acquisition and processing of

170 EDS spectra, at the School of Geoscience in Edinburgh. Working conditions during

171 acquisition of SEM backscatter images and during EDS analysis were 20 KV

172 acceleration voltage and a working distance of 6.9 mm. Chemical compositions, to be

173 correlated with the x-ray absorption coefficients, were measured on a Cameca SX100

174 electron microprobe at 20 kV acceleration voltage and a beam diameter of 3 µm, at the

175 University of Edinburgh. The microprobe is composed by 5 vertical crystal

176 spectrometers and a PGT Spirit energy dispersive analyser. Natural standards were

177 used. Further microprobe analyses were acquired at the EMPA at the University of

178 Munster, using a JEOL 8530F electron microprobe. The standard microprobe

179 conditions were 15 nA and 20 keV for quantitative analysis and 50 nA and 15 keV for

180 the element mapping. Standards used for quantitative measurement were jadeite (Na),

181 kyanite (Al), sanidine (K), olivine (Mg), hypersthene (Si), diopside (Ca), rhodocrosite

182 (Mn), rutile (Ti), fayalite (Fe), and chromite (Cr). Compositional maps were obtained

183 using XMapTools v. 2.3.1 (Lanari *et al.*, 2014).

184 Crystallographic orientations were measured on a Jeol 6610 SEM equipped with a

185 NordlysNano EBSD detector (Oxford Instruments) at the Plymouth University Electron

186 Microscopy Centre. Working conditions during acquisition of the EBSD patterns were

187 20 kV acceleration voltage, 70° sample tilt, high vacuum (in case of the carbon-coated

188 samples 0617 and 066B2), and low vacuum (30 Pa, in case of the uncoated sample

189 0618). EBSD patterns were acquired on rectangular grids with step sizes varying from

9

190   0.8 to 4.8 μm. All the thin sections were chemically polished with colloidal silica prior

191   to EBSD analysis. EBSD patterns were indexed with the AZtec software (Oxford

192   Instruments) and processed with Channel 5 software (Oxford Instruments). Raw EBSD

193   data were processed to reduce data noise following the procedure proposed by Prior *et*

194   *al.*, (2002) and Bestmann & Prior (2003). Crystallographic data were plotted on pole

195   figures as one point per grain. Pole figures are oriented with their horizontal diameter

196   corresponding to the trace of the mylonitic foliation (E-W). Crystallographic maps were

197   produced to highlight phase distribution (phase map), the internal misorientation of

198   grains (local misorientation map) and the crystallographic orientation of grains with

199   respect to specific direction of the kinematic reference frame (Inverse Pole Figure Map,

200   IPF).

201   **Synchroton x-ray microtomography**

202   X-ray absorption microtomographic data were collected at the beamline 2-BM at the

203   Advanced Photon Source (USA) using a monochromatic beam of 27 KeV and a low

204   sample-detector distance to minimise phase contrast. 1500 projections per dataset were

205   reconstructed into 3-dimensional image stacks using the gridrec algorithm (Rivers &

206   Wang, 2006). The voxel (i.e. a 3-dimensional pixel) side length of the reconstructed

207   data is 1.3 μm, which is sufficient to resolve the necessary petrographic details on the

208   μm-scale.

209   **Image Processing and Analysis**

210   The reconstructed x-ray absorption microtomographic datasets were filtered using an

211   Anisotropic Diffusion Filter 2D to reduce image noise (Tschumperlé & Deriche, 2005;

212   Schlüter *et al.*, 2014). Using the image processing software Fiji (Schindelin *et al.*,

213   2012), garnet was then segmented (i.e. numerically isolated) from the 3-dimensional

214   data using Statistical Region Merging followed by Global Thresholding (Nock &

215   Nielsen, 2004). Analysis of the resulting segmented images included the quantification

216   of garnet volumes and grain sizes, as well as a garnet interconnectivity analysis, all of

217   which were performed in Avizo Fire (v.8) (http://www.fei.com/software/avizo3d/)

218   using its Labelling and Label Analysis operators. Label analysis is a process that

219   identifies and evaluates face-connected clusters of voxels belonging to a specific class

220   (i.e. garnet) in segmented data. Face-connected voxel clusters do not represent

221   individual garnet grains but rather volumes occupied by garnet. Since X-ray absorption

222   microtomography does not detect grain boundaries in the garnet coronas, numerical

223   separation of the voxel clusters into individual grains is impossible in our data and we

224   are restricted to interpreting voxel clusters. To avoid introducing numerical shape

225   artefacts during the analyses of garnet, isolated voxel clusters with a volume smaller

226   than 125 cubic voxels (5x5x5 voxels, ~275 μm^3) were removed using the Analysis

227   Filter operator (see Fusseis *et al.*, 2012 for details).

228   In microtomographic data, volume calculations are affected by errors introduced by

229   the segmentation method (Arns *et al.*, 2002). To estimate the errors, we applied the

230   method described in Fusseis *et al*. (2012). Each segmented volume was both

231   numerically eroded and dilated by 1 voxel, and the resulting changes to the volume

232   and label analysis were quantified. The resulting quantifications are considered as

233   maximum possible errors.

234   Besides providing errors bars, binary data that have been eroded or dilated have the

235   potential to reveal details on the shape and spatial arrangement of voxel clusters, as

11

236   each morphological operation will cause voxel clusters to join, break up or disappear

237   altogether (see inset in Fig. 8). We analysed a version of the segmented garnet data

238   that underwent a single morphological erosion step. Morphological erosion removes

239   each voxel classified as garnet that is not completely surrounded by other voxels

240   classified the same. The erosion operator responds to the size and shape of the voxel

241   clusters, and the shortest diameter defines this response. The smallest unit that would

242   survive a morphological erosion step is a cubic array consisting of 3^3 voxels. A much

243   larger, spherical voxel cluster would retain its spherical shape through multiple erosion

244   steps. Oblate voxel clusters, which are characterised by one radius being substantially

245   shorter than others, will respond differently to erosion. Where cluster shapes are

246   irregular, morphological erosion will strangulate clusters at the shortest diameters (i.e.

247   the weakest links) and break them apart into several smaller ones, which is reflected

248   by a corresponding change in the cluster size distribution.

249   Using Avizo Fire, the 2-dimensional BSE images together with the EDS and EBSD

250   image data were reintroduced into 3-dimensional space to combine observations from

251   various sources with the microtomographic data into multidimensional datasets (Fig.

252   2). This allowed correlating x-ray absorption signals with chemical compositions and

253   crystallographic information and, as a result, extrapolating observations made by

254   electron microscopy to the third dimension.

255   **RESULTS**

256   **Petrological characterization**

257   In the *low strain domain*, at larger distance to the shear zone centre (sample #066B2),

258   although the magmatic gabbroic assemblage is still preserved, all mineral phases show

12

259 reaction textures (Fig. 3A). These reactions, related to sluggish kinetics, were triggered

260 by fluid-rock interactions: the amount of the reacted rock volume decreases with the

261 distance to the hydrous shear zone (Lund & Austrheim, 2003; John *et al.*, 2009).

262 Olivine cores ($Fo_{54}Fa_{45.6}Tep_{0.3}$) are surrounded by innermost coronas of fibrous

263 orthopyroxene followed by a ~ 50 µm wide poikiloblastic corona of garnet

264 ($Alm_{63.3}Grs_{19.8}Py_{14.9}$, Fig. 3A) and fibrous amphibole (Hornblende) at the contact with

265 plagioclase. The grain size of olivine cores is variable, generally of the order of a few

266 hundred micrometers. Olivine grains exhibit cleavage planes in different orientations.

267 While orthopyroxene coronas seem to have a constant width around olivine grains,

268 garnet coronas vary in thickness. These microfabrics are similar to the ones previously

269 described by Mørk, (1985), Krabbendam *et al.*, (2000), Lund & Austrheim (2003),

270 Müller (2013). According to Mørk (1985), the coronas between olivine and plagioclase

271 form through reaction: Ol + Pl (An) + Cpx + $H_2O \Rightarrow$ Opx + Grt + Am + Pl (Ab). It is

272 unclear whether these coronas formed as products of synkinematic fluid infiltration

273 (Krabbendam *et al.*, 2000; Lund & Austrheim, 2003), or as results of late-magmatic

274 processes (Mørk, 1986). However, we speculate that amphibole is indicative of the

275 external influx of hydrous fluids upon shear zone formation, as shown later by CPO of

276 hornblende in the high strain zone (Austrheim, 1987; Austrheim, *et al.*, 1997; Engvik *et*

277 *al.*, 2000; Labrousse *et al.*, 2004; Putnis & Austrheim, 2010).

278 Truly eclogite-facies assemblages are only observed at fluid pathways terminations or

279 where fluid availability and/or deformation enhanced the size of the reacted domains

280 allowing for sufficient material transport and thus bulk equilibration resulting in the

281 formation of an omphacite-garnet assemblage (Fig. 4) (Lund & Austrheim, 2003; John

282   *et al.*, 2009; Putnis & Austrheim, 2010). However, the overall dominance of amphibole

283   over omphacite in the samples indicates that the chemical equilibrium of the system was

284   local, and in favour of garnet-amphibole assemblage, instead of garnet and omphacite.

285   In those cases where plagioclase reacted in rather isochemical systems, the high-

286   pressure assemblage is dominated by the Ab-Czo symplectites ± amphibole ± garnet

287   (Lund & Austrheim, 2003; John *et al.*, 2009).

288

289   In the *intermediate strain domain* (sample #061751), the texture changes (Fig. 3C-3D).

290   Olivine grains are pseudomorphically replaced by orthopyroxene and orthoamphibole

291   intergrowth, which is surrounded by a thin (a few μm wide) rim of omphacite (Fig. 4B,

292   see also Lund & Austrheim, 2003). Mørk (1985) interprets the discontinuous growth of

293   thin omphacite layers between orthopyroxene and garnet coronas to have formed

294   through: (Ol) + Grt + Opx + Am + Pl $\Rightarrow$ Omp + Spin. However, the fact that, in contrast

295   to Mørk (1985), we did not observe spinel inclusions, points to this reaction being

296   incomplete in our samples, and mineral growth limited by material supply (see also

297   Mørk, 1985; John *et al.*, 2009). Clinopyroxene grains in this domain appear less regular

298   and altered by cloudy patches of Fe-Ti oxides as a result of destabilization through the

299   reaction: Cpx (Aug) + Na $\Rightarrow$ Na-Aug + Fe-Ti oxides, in which Na-Aug constitutes a

300   second generation of more altered clinopyroxene with increase Jd-component but

301   reduced Ti and Fe contents (Cpx$_2$) (Mørk, 1985). Garnet and amphibole are still present,

302   but they do not form clear corona structures anymore (see also Fig. 3B). The 3-

303   dimensional distribution of garnets still resemble coronas where decaying olivine grains

304   are more completely replaced by orthopyroxene, but generally garnet grains develop

14

305   euhedral crystals and form disconnected and more elongated aggregates (Fig. 7B).

306   Towards the shear zone, all plagioclase is replaced by clinozoisite and albite symplectites

307   through the reaction (Fig. 4B, C): Pl (An) + $H_2O \Rightarrow$ Czo + Ab symplectites (Wayte *et al.*,

308   1989; Lund & Austrheim, 2003; John *et al.*, 2009; Müller, 2013) (Fig. 4). The Czo+Ab

309   symplectites are preserved without evidence of any later overprint, and we consider them

310   to have formed as prograde replacement of plagioclase in a fluid-mediated system,

311   indicating a metastable prograde reaction (Wayte *et al.*, 1989). Therefore, in the presence

312   of amphibole, omphacite associated with these delicate symplectite textures indicates a

313   prograde conversion of the gabbro to an eclogite in which fluid infiltration was

314   synkinematic and linked to the progress of reaction and deformation (Fig. 4B).

315

316   In the *most deformed sample* (#0618), all mineral phases are aligned parallel to a

317   mylonitic foliation. The foliation is defined by a compositional layering of elongated

318   orthopyroxene-amphibole symplectites, and garnet, forming isolated elongated clusters

319   >100 μm wide and several hundred μm long (Fig. 3E-3F). Some of garnet grains still

320   exhibit faceted crystals (Fig. 7C).

321   Omphacite is present at the margins of relict magmatic clynopyroxene grains and of

322   orthopyroxene-amphibole symplectites (Fig. 4C).

323

324   **Garnet chemical composition**

325   Garnet compositions in the three samples were measured using electron microprobe

326   analyses in order to confirm the chemical evolution of garnet with respect to the

327   deformation history (Fig. 5, 6; Tab. S3). With increasing deformation, garnet

328 compositions become more Alm-rich (Fig. 5), an expected trend for a gabbro that is

329 gradualy equilibrating under eclogite-facies P-T conditions. Within the low-strain

330 domain, high CaO concentrations (X_{Grs}) are represented by garnet in the proximity of

331 Ca-rich phases (e.g. plagioclase). In the high strain domain the compositional maps

332 show that some garnet displays CaO zoning (5-12 wt. %) and zoning pattern similar to

333 those observed in low strain domain (Fig. 6). It seems that locally these garnets

334 represent collapsed former coronas (a', b' in Fig. 6C).

335 Furthermore, fine-grained garnets (Fig. 6C to the left) represent highly fragmented and

336 collapsed former coronas.

337

338 **4D spatial evolution of garnet grains**

339 A subvolume with dimensions of 600^3 voxels (~0.5 mm^3) was extracted from each of the

340 three microtomographic datasets to visualize the 3-dimensional distribution of garnet

341 (Fig. 7). In the subsequent label analysis, garnet distribution was evaluated and

342 quantified in the original, statistically representative 7 mm^3 subvolumes (Fig. 3, 9). In the

343 label analysis, we considered all garnet clusters that consist of face-connected voxels and

344 are larger than 125 cubic voxels (~ 275 μm^3). This allowed us to relate the following

345 observations to the 3-dimensional petrography presented above.

346 The volumetric quantification of the segmented garnet data shows that the garnet volume

347 increases into the shear zone, from 6 % (± 2.5 %) in the low-strain sample, to 11 % (± 3

348 %) in the intermediate strain sample, and 20 % (± 4 %) in the high-strain sample.

349

350 The visualisation confirms that in the *low strain domain*, garnet forms voluminous

351 interconnected coronas around orthopyroxene and decaying olivine grains (Fig. 7). It also

352 becomes apparent that different olivine cores have garnet rims with different thicknesses.

353 Measurements of garnet corona thicknesses around five different olivine grains show an

354 average thickness of 60 μm with standard deviations that vary from 10 to 35 μm in the

355 most complex coronas. Where two olivine grains neighbour each other, garnet coronas

356 become almost twice as thick. There seems to be no correlation between the thickness of

357 the garnet- and the amphibole rims, which should have evolved in unison (Mørk, 1985;

358 Mørk, 1986; Johnson & Carlson, 1990). Despite their considerable spatial extent, garnet

359 coronas do not enclose olivine grains entirely, which leaves dormant reactants in direct

360 contact with each other (Figure S9). The resulting baseball-glove shaped domains also do

361 not show any preferential spatial orientation with respect to the kinematic framework of

362 the shear zone (Figure S9). The total garnet volume in the analysed subvolume is

363 accommodated by 1116 garnet voxel clusters (Table S3).

364 The label analysis shows that the garnet population is dominated by one large

365 interconnected garnet voxel cluster that percolates across the entire subvolume (Fig. 9A).

366 This cluster accounts for 83 % of the entire garnet volume in the sample (Fig. 8A, B).

367 Garnet voxel clusters between $2.2*10^6$ and $3.08*10^7$ μm^3 account for 11%, whereas voxel

368 clusters $< 2.2*10^6$ μm^3 do not contribute substantially to the total garnet volume (Fig.

369 8B).

370 We submitted the segmented data to a numerical volume erosion process to learn more

371 about the spatial arrangement of garnet (see supplementary data for details on the

372 procedure and Table S4 for the results). Garnet interconnectivity persists through the

373 volume erosion, which evidences how tightly individual garnets grains are linked in the

17

374   coronas (see suppl. material for details). In the eroded data, the garnet volume forms

375   2796 voxel clusters (Table S4). The largest interconnected voxel cluster dramatically

376   decreases in volume from $4*10^8$ μm^3 to 10^8 μm^3, now accounting for only 35 % of the

377   total volume. The eight largest interconnected voxel clusters (> $2.2*10^6$ μm^3) account for

378   89 % of the total garnet volume as seen in the cumulative frequency diagram (Fig. 8B).

379   The erosion process also leads to a substantial increase in frequency for sizes smaller

380   than 10^4 cubic μm^3 (Fig. 8A), which is in contrast to the intermediate and high-strain

381   datasets.

382

383   The visualisation of garnet in the *intermediate strain domain* shows that the larger garnet

384   voxel clusters form complexly-shaped rims around orthopyroxene aggregates that likely

385   have their origin in former coronas (Fig. 9B). In this sample, the garnet volume is made

386   up of 12068 garnet voxel clusters. This almost ten-fold increase over the low strain

387   sample is essentially being accommodated by the smallest (< 10^5 μm^3) and largest (>

388    $6*10^8$ μm^3) voxel cluster size fractions (Table S3). A similar number of voxel clusters in

389   the size region of 10^5 μm^3 was detected, whilst a particularly large number of voxel

390   clusters with volumes between 10^3 and 10^4 μm^3 were found. Again, the largest 10 voxel

391   clusters (> $2.2*10^6$ μm^3) account for over 90 % of the total garnet volume. The largest

392   interconnected voxel cluster, which is larger than in the low-strain sample (from $4*10^8$

393   μm^3 to $6.5*10^8$ μm^3) develops through the subvolume and accounts for 80 % of the total

394   garnet volume. The garnet voxel clusters in the range of $2.6*10^5$ to $4*10^6$ μm^3 are often

395   formed by isolated, euhedral and potentially newly formed garnet grains (Fig. 7, 9B; see

396   Discussion). Voxel clusters smaller than 10^5 μm^3 are arranged in patchy clouds

18

397   surrounding bigger interconnected voxel clusters.

398   In the numerically eroded data, the number of garnet voxel cluster reduces to 4995. Since

399   a numerical erosion cannot lead to voxel cluster coalescence, this decrease reflects a

400   sensitivity to the disappearance of volumetrically small voxel clusters in the procedure

401   (Fig. 8C, Table S4). In the erosion process, the largest voxel cluster breaks apart to form

402   two smaller voxel clusters, which together account for 70 % of total garnet volume (Fig.

403   8D, Fig. S10).

404

405   The visualization of the microtomographic data shows that in the most deformed sample,

406   the garnet voxel clusters define a mylonitic foliation. In this subvolume, garnets

407   contribute to a deformation microfabric; the garnet voxel clusters define the

408   compositional layering observed in the SEM analysis (Fig. 9C). Additional analyses that

409   we conducted (using the software package Quant3D, Ketcham & Ryan (2004)) revealed

410   that most of the garnet voxel clusters in this sample have an oblate shape (Fig. S11).

411   Garnet in the subvolume is organized in 9297 voxel clusters (Table S3). A total of 46

412   voxel clusters have a volume larger than $2.2*10^6$ μm^3, and they account for 86 % of the

413   total garnet volume (Fig. 8F). The absolute frequency-size distribution is self-similar,

414   with no major local variations between the size classes. This trend is confirmed by the

415   cumulative plot (Fig. 8F), which shows that all size classes contribute progressively

416   towards the total garnet volume, and is in contrast to the other two samples.

417   Numerical erosion reduces the number of garnet voxel clusters to 8014, of which 62 are

418   larger than $2.2*10^6$ μm^3 and accommodate 81 % of garnet total volume (Table S4). The

419   reduction in total voxel cluster number is accommodated by all size fractions, which

19

420   indicates that the voxel clusters have shapes that withstand a numerical erosion process

421   (Fig. 8E, F).

EBSD analysis: Misorientation of garnet grains in the shear zone

423   We analysed predominantly garnet in the three samples using EBSD to investigate the

424   dominant deformation mechanisms that contributed towards the evolution of the

425   microfabric in garnets.

426   Garnet and orthopyroxene in the *low strain sample* exhibit frequent low angle

427   boundaries (misorientation between 3° and 10°). The phase map of a coronitic domain

428   around magmatic olivine shows that orthopyroxene and hornblende grows as fibrous

429   crystals: the long axis of orthopyroxene and hornblende are perpendicular to the

430   reaction interface (Fig. S3A). In the case of hornblende, the elongation is parallel to the

431   <001> axis (Fig. S4F). The inverse pole figure map (IPF) of garnet, shown with respect

432   to the E-W direction (i.e. approximately equivalent to the normal to the reaction

433   interface and parallel to the elongation direction of hornblende) (Fig. 10A), highlights

434   the presence of low-angle boundaries, which correspond, in the local misorientation

435   map (Fig. S3C), to internal misorientation zones with up to 9° of misorientation in

436   garnet. A misorientation profile across them does not show any progressive distortion

437   of the crystal lattice, but rather a sudden jump in misorientation (Fig. 10B). The

438   average local internal misorientation of grains is very low, on the order of 1°, i.e. within

439   the error of measurement. The misorientation axes for misorientation angles of 3-10°

440   do not show clear maxima in crystal coordinates (Fig. 10C). Pole figures show that

441   coronitic garnet grains are not elongated parallel to specific crystallographic directions

442   (Fig. S3B, S4E).

20

443   In the *intermediate strain sample* the spatial density of low angle boundaries is highly

444   variable. A local misorientation map shows that the interiors of garnet grains are

445   virtually undeformed (average local misorientation on the order of 1°), and that there

446   are bands with high misorientation up to 9° (Fig. 10D). A misorientation profile across

447   one of the bands shows a rather abrupt misorientation jump (of up to 8°) (Figure 10E).

448   Similar to the low strain domain, the misorientation axes for misorientation angles of 3-

449   10° do not show clear maxima in crystal coordinates (Figure 10F). The IPF map and

450   the associated pole figures show a weak preferred orientation of garnet, with voxel

451   clusters of grains preferentially oriented with their <111> parallel to the stretching

452   lineation of the shear zone (Fig. S5A, S5E). The IPF map shows that garnet grains

453   range in size between 10-20 µm and 200 µm.

454   In the *high strain sample*, the density of low angle boundaries in garnet is very low, and

455   they are typically present only in grains larger than 50 µm (Figure 10G). The phase

456   map indicates that individual garnet grains range in size from ca. 10 µm to ca. 150-200

457   µm and are dispersed in a matrix of hornblende, orthopyroxene and minor biotite (Fig.

458   S6A). Garnet grains are internally strain-free (average local misorientation is < 1°), and

459   again, there is no progressive accumulation of misorientation towards the few internal

460   high misorientation bands (as indicated by the local misorientation map in Fig. S6B).

461   Less frequently, a progressive accumulation of lattice distortion (of up to 4°) towards

462   the low angle boundaries was observed (Fig. 10H). The misorientation axes for

463   misorientation angles of 3-10° do not show clear maxima in crystal coordinates (Fig.

464   10I). Pole figures of garnet show only weak maxima of <100>, one of which is oriented

465   subparallel to the stretching lineation (Fig. S6C, S7A, S7B). Neighbouring grains are

21

466   typically characterized by large misorientations (>30°, Fig. S6F).

467   In contrast, hornblende shows a crystal preferred orientation (CPO) with the c-axis

468   oriented subparallel to the stretching lineation. This CPO of hornblende has been

469   commonly observed in lower crustal shear zones where hornblende grew

470   synkinematically to deformation (Berger & Stünitz, 1996; Getsinger & Hirth, 2014;

471   Menegon *et al.*, 2015).

472   We emphasize that, combined, the crystallographic data point to a negligible

473   contribution of crystal plasticity to garnet deformation.

474   **DISCUSSION**

475   **Strain-dependent evolution of garnet microfabrics in the Kråkeneset shear zone**

476   The observations reported above allow to draw a detailed picture of the synkinematic

477   evolution of garnet in this deep-crustal shear zone. Our microtomographic data indicate

478   that, across the studied shear zone margin, from low to high strain, garnets evolve from

479   a highly interconnected coronitic texture to a tectonic microfabric, where they are

480   organized in oblate aggregates and define the foliation of the shear zone (Fig. 9C).

481   Simultaneously, the garnet volume in the rocks more than triples. Based on chemical

482   analyses, which revealed a partial local equilibration of garnets grains at eclogite facies

483   (Fe-rich), we interpret the oblate sheared aggregates as having formed by the

484   progressive, synkinematic disintegration and rearrangement of coronas in combination

485   with the simultaneous nucleation and coalescence of garnets grains at similar P, T, X

486   metamorphic conditions (Fig. 11).

487   We argue that the garnet coronas originally formed as the high-pressure reaction

22

488   products of a prograde metastable reaction between olivine and plagioclase by the

489   coalescence of nuclei. As strain localises in the shear zone, these garnet coronas are

490   broken apart and start to disintegrate (Fig. 11-1, 11-2). At this stage, the garnet voxel

491   clusters do not reflect a deformation microfabric yet, and the largest garnet cluster is

492   still interconnected through the entire sample forming complexly-shaped rims around

493   orthopyroxene porphyroclasts that have replaced olivine. New garnet grains nucleate in

494   between these large voxel clusters but are still small at this stage, while existing garnet

495   grains are overgrown and increase in volume. At the highest level of strain, the former

496   garnet coronas have been deformed and re-arranged by granular flow in a ductively

497   deforming matrix, leading to a mylonitic deformation microfabrics defined by oblate

498   garnet voxel clusters (Fig. 3, 9 C).

499   *Where does all the garnet go?*

500   The results of the label analysis, and in particular the evolution of different size classes

501   of garnet voxel clusters, reveal how the volumetric increase in garnet is accommodated

502   and what processes affect the garnet population across the shear zone margin. The

503   overall increase in the number of garnet voxel clusters into the shear zone reflects the

504   synkinematic formation of a well-dispersed garnet population (Fig. 8). This is achieved

505   by the coeval activity of three processes, the fragmentation and breakup of garnet

506   coronas, the formation of overgrowth rims, and the nucleation of new garnet crystals

507   (Fig. 11):

508   1. The increase in the number of garnet voxel clusters, particularly the large ones,

509   with increasing strain clearly reflects a reduction of garnet interconnectivity. The

510   largest voxel cluster in the low and intermediate strain domain accounts for ~80

511   % of the overall garnet volume, whereas a similar volume proportion is

512   accommodated by 46 voxel clusters (> $2.2*10^6$ μm^3) in the most deformed

513   sample.

514   2. The transition from the low strain- to the intermediate strain domain sees a

515   complete reorganisation in the population of the smallest garnet voxel clusters

516   (Fig. 8C). Voxel clusters $\leq 4.1*10^3$ μm^3 increase in number from 698 to 11239

517   (Table S3). These clusters occur dispersed in between the larger clusters, without

518   any obvious textural link. As the total amount of garnet volume increases, they

519   cannot be fragments of initial coronitic garnet, therefore we argue that this

520   population of smallest voxel clusters is the product of nucleation and speculate

521   that these garnets may evidence pervasive fluid infiltration (see following

522   section).

523   3. In contrast, we infer the increase in the number of intermediate-sized voxel

524   clusters with volumes between $2.6*10^5$ and $4*10^6$ μm^3, which is particularly

525   apparent in the intermediate strain domain, to be related to overgrowth. The 3-

526   dimensional visualisation shows that garnet voxel clusters have euhedral or semi-

527   euhedral shapes, which is congruent with this mechanism (Padrón-Navarta *et al.*,

528   2008).

529   *What the morphological operator "Erosion" reveals about the garnet distribution*

530   The frequency diagrams reveal that the number of voxel clusters does increase as a

531   response to erosion in the *low strain domain* for smaller voxel cluster sizes (< 10^4 μm^3,

532   Fig. 8A, B) and in the *intermediate strain domain* for the largest interconnected cluster

533   (Fig. S9). This indicates that a substantial number of voxel clusters exhibit cross-

534   sectional diameters short enough to respond to a single erosion step. By acting as

535   predetermined breaking points, these weak bridges become crucial in the disintegration

536   of the garnet coronas as the rock transitions to the intermediate strain microfabrics (see

537   also Fig. 11A). We infer that the larger proportion of the garnet volume that is

538   accommodated by smaller clusters in the eroded dataset (Fig. 8B) is a consequence of

539   this break-up.

540   In the *intermediate strain domain*, the absolute frequency of voxel clusters $<5*10^4$ µm^3

541   decreases significantly as a consequence of morphological erosion (Figure 8C, Tables

542   S3, S4). These are the voxel clusters that make up the patchy clouds in between the

543   larger garnet aggregates. Many of these small clusters are apparently susceptible to

544   annihilation in a single erosion step, which points towards a significant deviation from

545   sphericity in this voxel cluster population.

546   In the *high strain domain*, the garnet voxel clusters retain their self-similar frequency-

547   size distribution through the morphological erosion process in the high strain domain

548   (Fig. 8E, F). However, the changes to the frequency of voxel clusters in the different

549   bins seem to reflect a slight decrease in the fractal dimension (Fig. 8E, F). A new

550   population of voxel clusters with volumes $<10^3$ µm^3 is generated from larger clusters,

551   and the largest voxel cluster halves in size (from 1.1 to $2.2*10^8$ µm^3).

552   *Micromechanisms involved*

553   Our EBSD data indicate that the mechanism by which the garnet coronas are

25

554   disintegrated does not involve crystal plasticity by means of dislocation activity. Whilst

555   garnet was shown to deform by dislocation creep at upper amphibolite to granulite

556   facies metamorphic conditions (Ji & Martignole, 1994; Ji & Martignole, 1996), this was

557   not the case in the sampled shear zone. Misorientation maps and profiles indicate that

558   neighbouring garnet domains show only limited and relative rotations (Fig. 10). These

559   motions are accommodated by narrow, distinct bands that correspond to low-angle

560   boundaries; the grains themselves show very little internal deformation. The bands

561   coincide with sudden jumps in misorientations, testifying that they are not subgrains or

562   dislocation walls (Fig. 10B, E, H, e.g. Viegas *et al.*, (2016)). Furthermore, the plots of

563   misorientation axis in crystal coordinates show that the low-angle boundaries are not

564   tied to the host crystallography but rather show a highly dispersed distribution (Fig.

565   10C, F, I). Based on these arguments, we suggest that the low angle boundaries in the

566   low strain domain are growth features, and probably related to an early stage of

567   coalescence of nuclei. The overall lack of chemical differences amongst the newly

568   formed garnets and their seeds would be congruent with a close initial nucleation

569   spacing of garnets seeds, similar to the observations reported in Whitney & Seaton

570   (2010).

571   On the basis of an almost complete lack of evidence for crystal plasticity, we argue that

572   the progressive disintegration and rearrangement of garnet coronas was accommodated

573   by microfracturing and passive granular flow of garnets in a viscously deforming

574   matrix (cfr. Trepmann & Stöckhert, 2002). This view is supported by experimental

575   data on garnet rheology (Voegelé *et al.*, 1998; Wang & Ji, 1999; Zhang & Green,

576   2007), which establish the possibility of brittle garnet behaviour at the inferred

26

577   metamorphic conditions.

578   Microfracturing and passive granular flow of garnet grains could have been assisted by

579   a fluid phase (Den Brok & Kruhl, 1996; Storey & Prior, 2005; Smit *et al.*, 2011). As it

580   is well established, fluid infiltration played a critical role in triggering eclogitization and

581   strain localisation in dry and ridged precursor rocks (Austrheim, 1987; Austrheim *et al.*,

582   1997; Engvik *et al.*, 2000; John & Schenk, 2003; Miller *et al.*, 2007; Labrousse *et al.*,

583   2010; Putnis & John, 2010). The presence of fluids in the system is evident from the

584   hydrous high-pressure mineral assemblage in the shear zone. However, we found no

585   clear evidence for fluid-assisted deformation mechanisms, such as intergranular

586   pressure solution (e. g. Azor *et al.*, (1997), Smit *et al.*, (2011)), diffusion creep (Den

587   Brok & Kruhl, 1996; Storey & Prior, 2005) or grain-boundary sliding and diffusion

588   creep (Terry & Heidelbach, 2004) to have dominated garnet deformation. However, we

589   do interpret garnet to trace fluid migration pathways to some extent (see following

590   subsection).

591   **Implications for fluid flow, mass- and element transport**

592   The 3-dimensional spatial arrangement of garnets is not only the results of deformation,

593   but, in the low-strain domain, it also reflects mass transport between plagioclase and

594   olivine grains during their reaction (Austrheim, 1987; Lund & Austrheim, 2003;

595   Labrousse *et al.*, 2010; Putnis & John, 2010). Our observations show that garnet

596   coronas are highly interconnected throughout the low strain samples (Fig. 9A) and thus,

597   fluid transport must have happened on a trans-granular scale. However, the coronas do

598   not encapsulate and isolate olivine grains from plagioclase, as commonly thought when

599   observing coronas in two dimensions (Mørk, 1986; Johnson & Carlson, 1990; Keller *et*

600   *al.*, 2004). Where the coronas did not form, this happened despite the reactants being in

601   direct contact with each other, and obviously the reaction was subdued. We argue that

602   garnet formed where fluids facilitated the reaction and we therefore link the

603   heterogeneously distributed reaction products to fossilized fluid pathways.

604   In the intermediate strain domain, syn-reactive fluid-infiltration is testified by the

605   presence of cloudy patches of small garnets, along with the observation that water-

606   bearing minerals are concentrated in the shear zone centre. The abundance of these

607   minerals decreases along the lateral strain gradient away from the shear zone and are

608   absent where the gabbro is undeformed (John *et al.*, 2009). These observations are

609   congruent with those reported in earlier studies by Austrheim (1987), Wayte *et al.*,

610   (1989), Engvik *et al.* (2001), John & Schenk (2003), and Putnis & John (2010). These

611   studies established that eclogitization in the lower crust can be triggered by an external

612   input of fluids and facilitated by the presence of preferential pathways, such as

613   fractures, which controlled element mobility and defined reaction pathways. However,

614   our data also reveal that there is no systematic arrangement of the garnet coronas with

615   respect to a kinematic framework defined by the deformation microfabrics. It therefore

616   remains unclear what controlled preferential fluid pathways on the grain scale.

617   In an extension to this argument, we claim that in the high-strain samples, the oblate

618   garnet aggregates also should have channelized synkinematic fluid flow (see also

619   Austrheim (1987)). We interpret the aligned, oblate garnet aggregates, defining the

620   foliation, as having acted as fluid barriers and thereby direct synkinematic fluid flow in

621   the shear zone.

622 **CONCLUSIONS**

623 4-dimensional quantitative x-ray micro-tomography proved to be an excellent approach

624 to investigate the evolution of metamorphic reaction microfabrics in three dimensions.

625 In combination with established microanalytical methods, it allowed a comprehensive

626 characterization of the processes affecting the evolution of garnet during eclogitization

627 in a shear zone in the Western Gneiss Region, Norway. In particular, we were able to:

628 • Capture and monitor the spatial distribution of mineral phases in four dimensions:

629 the x-ray absorption contrast between individual mineral phases in our micro-

630 tomographic data is sufficient to allow the same petrographic observations than in light-

631 and electron microscopy, but extended to the 3rd and, where strain is considered a proxy

632 for time, 4th dimension.

633 • Quantify the change in garnet volume across the strain gradient: with increasing

634 deformation, the garnet volume increases from about 6 % to 20 %.

635 • Determine the interconnectivity of garnet grains as a function of strain, with

636 implication for mass transport, syn-reactive fluid flow and rock strength.

637 • Identify the 3-dimensional geometry of garnet coronas, find that they do not

638 encapsulate olivine grains and have no apparent preferred alignment. We interpret the

639 garnet coronas to outline fossilized fluid pathways.

640 • Identify the mechanisms by which garnet is reorganised during shearing:

641 microfracturing, nucleation and overgrowth. We interpret these observations as pointing

642 to a mechanical disintegration of garnet coronas during strain localisation and their

643   rearrangement into individual sheared isolated voxel clusters, with the ongoing

644   nucleation of new garnets and overgrowth while the rock was deforming. There is no

645   evidence for crystal plastic deformation, all garnets are internally strain free and in the

646   more deformed samples they show a very weak crystal preferred orientation.

647   Our study clearly shows what 3- or 4-dimensional datasets from reaction micro-fabrics

648   can add to the understanding of metamorphic processes. We reiterate that a 2-

649   dimensional analysis of deformation microfabrics can lead to incorrect petrological and

650   structural interpretations, and it does omit information that only become available when

651   rocks are investigated in three dimensions.

661 **REFERENCES**

662 Aerden, D., 2005. Comment on "Reference frame, angular momentum, and

663   porphyroblast rotation" by Dazhi Jiang and Paul F. Williams. *Journal of Structural*

664   *Geology*, **27**, 1128–1133.

665 Ague, J.J. & Carlson, W.D., 2013. Metamorphism as garnet sees it: The kinetics of

666   nucleation and growth, equilibration, and diffusional relaxation. *Elements*, **9**, 439–

667   445.

668 Arns, C.H., Knackstedt, M. a., Pinczewski, W.V. & Garboczi, E.J., 2002. Computation

669   of linear elastic properties from microtomographic images: Methodology and

670   agreement between theory and experiment. *Geophysics*, **67**, 1396.

671 Austrheim, H., 1987. Eclogitization of lower crustal granulites by fluid migration

672   through shear zones. *Earth and Planetary Science Letters*, **81**, 221–232.

673 Austrheim, H., Erambert, M. & Engvik, A.K., 1997. Processing of crust in the root of the

674   Caledonian continental collision zone: the role of eclogitization. *Tectonophysics*,

675   **273**, 129–153.

676 Azor, A., Simancas, J.F., Exposito, I., Lodeiro, F.G. & Martinez Poyatos, D.J., 1997.

677   Deformation of garnets in a low-grade shear zone. *Journal of Structural Geology*,

678   **19**, 1137–1148.

679 Baxter, E.F. & Scherer, E.E., 2013. Garnet geochronology: Timekeeper of

680   tectonometamorphic processes. *Elements*, **9**, 433–438.

681 Bell, T.H. & Johnson, S.E., 1989. The role of deformation partitioning in the deformation

682   and recrystallization of plagioclase and K-feldspar in the Woodroffe Thrust

683   mylonite zone, central Australia. *Journal of Metamorphic Geology*, **7**, 151–168.

684   Berger, A. & Stünitz, H., 1996. Deformation mechanisms and reaction of hornblende:

685   examples from the Bergell tonalite (Central Alps). *Tectonophysics*, **257**, 149–174.

686   Bestmann, M. & Prior, D.J., 2003. Intragranular dynamic recrystallization in naturally

687   deformed calcite marble: Diffusion accommodated grain boundary sliding as a

688   result of subgrain rotation recrystallization. *Journal of Structural Geology*, **25**,

689   1597–1613.

690   Boundy, T.M. Fountain, D.M., & Austrheim, H., 1992. Structural development and

691   petrofabrics of eclogite facies shear zones, Bergen Arcs, western Norway:

692   implications for deep crustal deformational processes. *Journal of Metamorphic*

693   *Geology*, **10**, 127–146.

694   Den Brok, B. & Kruhl, J.H., 1996. Pergamon Ductility of garnet as an indicator of

695   extremely high temperature deformation. *Journal of Structural Geology*, **16**, 985–

696   996.

697   Carlson, D.W., 2011. Porphyroblast crystallization: linking processes, kinetics, and

698   microstructures. *International Geology Review*, **53**, 406–445.

699   Carlson, W.D. & Johnson, C.D., 1991. Coronal reaction textures in garnet amphibolites

700   of the Llano Uplift. *American Mineralogist*, **76**, 756–772.

701   Cuthbert, S.J., Carswell, D.E.A., Krogh-Ravna, E.J. & Wain, A., 2000. Eclogites and

702   eclogites in the Western Gneiss region, Norwegian Caledonides. *Lithos*, **52**, 165–

703   195.

704   Denison, C. & Carlson, W.D., 1997. Three-dimensional quantitative textural analysis of

705   metamorphic rocks using high-resolution computed X-ray tomography : Part II .

706   Application to natural samples. *Journal of Metamorphic Geology*, **15**, 45–57.

707   Dobbs, H.T., Peruzzo, L., Seno, F., Spiess, R. & Prior, D.J., 2003. Unraveling the

708   Schneeberg garnet puzzle: A numerical model of multiple nucleation and

709   coalescence. *Contributions to Mineralogy and Petrology*, **146**, 1–9.

710   Engvik, A.K., Austrheim, H. & Andersen, T.B., 2000. Structural, mineralogical and

711   petrophysical effects on deep crustal rocks of fluid-limited polymetamorphism,

712   Western Gneiss Region, Norway. *Journal of the Geological Society*, **157**, 121–134.

713   Engvik, A.K., Austrheim, H. & Erambert, M., 2001. Interaction between fluid flow,

714   fracturing and mineral growth during eclogitization, an example from the Sunnfjord

715   area, Western Gneiss Region, Norway. *Lithos*, **57**, 111–141.

716   Fusseis, F. & Handy, M.R., 2008. Micromechanisms of shear zone propagation at the

717   brittle-viscous transition. *Journal of Structural Geology*, **30**, 1242–1253.

718   Fusseis, F., Handy, M.R. & Schrank, C., 2006. Networking of shear zones at the brittle-

719   to-viscous transition (Cap de Creus, NE Spain). *Journal of Structural Geology*, **28**,

720   1228–1243.

721   Fusseis, F., Schrank, C., Liu, J., Karrech, A., Llana-Fúnez, S., Xiao, X. & Regenauer-

722   Lieb, K., 2012. Pore formation during dehydration of a polycrystalline gypsum

723   sample observed and quantified in a time-series synchrotron X-ray micro-

724   tomography experiment. *Solid Earth*, **3**, 71–86.

725   Getsinger, A.J. & Hirth, G., 2014. Amphibole fabric formation during diffusion creep

726   and the rheology of shear zones. *Geology*, **42**, 535–538.

727   Goergen, E.T. & Whitney, D.L., 2012. Corona networks as three-dimensional records of

728   transport scale and pathways during metamorphism. *Geology*, **40**, 183–186.

729   Hacker, B.R. & Andersen, T.B., 2010. High-temperature deformation during continental-

730   margin subduction and exhumation: The ultrahigh-pressure Western Gneiss Region

731   of Norway. *Tectonophysics*, **480**, 149–171.

732   Ji, S. & Martignole, J., 1996. Ductility of garnet as an indicator of extremely high

733   temperature deformation: reply. *Journal of Structural Geology*, **18**, 1375–1379.

734   Ji, S. & Martignole, J., 1994. Pergamon Ductility of garnet as an indicator of extremely

735   high temperature deformation. *Journal of Structural Geology*, **16**, 985–996.

736   Jiang, D. & Williams, P.F., 2004. Reference frame, angular momentum, and

737   porphyroblast rotation. *Journal of Structural Geology*, **26**, 2211–2224.

738   John, T., Medvedev, S. & Rüpke, L.H., 2009. Generation of intermediate-depth

739   earthquakes by self-localizing thermal runaway. *Nature Geoscience*, **2**, 137–140.

740   John, T. & Schenk, V., 2003. Partial eclogitisation of gabbroic rocks in a late

741   Precambrian subduction zone (Zambia): prograde metamorphism triggered by fluid

742   infiltration. *Contributions to Mineralogy and Petrology*, **146**, 174–191.

743   Johnson, S.E., 1993. Testing models for the development of spiral-shaped inclusion trails

744   in garnet prphyroblasts: to rotate or not to rotate, that is the question. *Journal of*

745   *Metamorphic Geology*, **11**, 635–659.

746   Johnson, C.D. & Carlson, W.D., 1990. The origin of olivine-plagioclase coronas in

747   metagabbros from the Adirondack Mountains, New York. *Journal of Metamorphic*

748   *Geology*, **8**, 697–717.

749   Keller, L.M., Abart, R., Stünitz, H. & De Capitani, C., 2004. Deformation, mass transfer

750   and mineral reactions in an eclogite facies shear zone in a polymetamorphic

751   metapelite (Monte Rosa nappe, western Alps). *Journal of Metamorphic Geology*,

752   **22**, 97–118.

753   Ketcham, R.A., 2005. Computational methods for quantitative analysis of three-

754   dimensional features in geological specimens. *Geosphere*, **1**, 32-41.

755   Ketcham, R.A. & Ryan, T.M., 2004. Quantification and visualization of anisotropy in

756   trabecular bone. *Journal of microscopy*, **213**, 158–71.

757   Konrad-Schmolke, M., Handy, M.R., Babist, J. & O'Brien, P.J., 2005. Thermodynamic

758   modelling of diffusion-controlled garnet growth. *Contributions to Mineralogy and*

759   *Petrology*, **149**, 181–195.

760   Krabbendam, M. & Dewey, J.F., 1998, Exhumation of UHP rocks by transtension in the

761   Western Gneiss Region, Scandinavian Caledonides. *Geological Society, London*,

762   *Special Publications*, **135**, 159–181.

763   Krabbendam, M., Wain, A. & Andersen, T.B., 2000. Pre-Caledonian granulite and

764   gabbro enclaves in the Western Gneiss Region, Norway: indications of incomplete

765   transition at high pressure. *Geological Magazine*, **137**, 235–255.

766   Labrousse, L., Hetényi, G., Raimbourg, H., Jolivet, L. & Andersen, T.B., 2010. Initiation

767   of crustal-scale thrusts triggered by metamorphic reactions at depth: Insights from a

768   comparison between the Himalayas and Scandinavian Caledonides. *Tectonics*, **29**,

769   1–14.

770   Labrousse, L., Jolivet, L., Andersen, T.B., Agard, P., Hebert, R., Maluski, H. & Scharer,

771   U., 2004. Pressure-temperature-time deformation history of the exhumation of ultra-

772   high pressure rocks in the Western Gneiss Region , Norway. *Geological Society of*

773   *America*, **380**, 155–183.

774   Lanari, P., Vidal, O., De Andrade, V., Dubacq, B., Lewin, E., Grosch, E.G. & Schwartz,

775   S., 2014. XMapTools: A MATLAB©-based program for electron microprobe X-ray

776   image processing and geothermobarometry. *Computers and Geosciences*, **62**, 227–

777   240.

778   Lund, M.G. & Austrheim, H., 2003. High-pressure metamorphism and deep-crustal

779   seismicity: evidence from contemporaneous formation of pseudotachylytes and

780   eclogite facies coronas. *Tectonophysics*, **372**, 59–83.

781   Martelat, J.E., Malamoud, K., Cordier, P., Randrianasolo, B., Schulmann, K. &

782   Lardeaux, J.M., 2012. Garnet crystal plasticity in the continental crust, new example

783   from south Madagascar. *Journal of Metamorphic Geology*, **30**, 435–452.

784   Massey, M. A., Prior, D.J. & Moecher, D.P., 2011. Microstructure and crystallographic

785   preferred orientation of polycrystalline microgarnet aggregates developed during

786   progressive creep, recovery, and grain boundary sliding. J*ournal of Structural*

787   *Geology*, **33**, 713–730.

788   Means, W.D., 1995. Shear zones and rock history. *Tectonophysics*, **247**, 157–160.

789   Menegon, L., Fusseis, F., Stünitz, H. & Xiao, X., 2015. Creep cavitation bands control

790   porosity and fluid flow in lower crustal shear zones. *Geology*, **43**, 227–230.

791   Miller, C., Zanetti, A., Thoni, M. & Konzett, J., 2007. Eclogitisation of gabbroic rocks:

792   Redistribution of trace elements and Zr in rutile thermometry in an Eo-Alpine

793   subduction zone (Eastern Alps). *Chemical Geology*, **239**, 96–123.

794   Mørk, M.B.E., 1985. A gabbro to eclogite transition on Flemsoy, Sunnmore, Western

795   Norway. *Chemical Geology*, **50**, 283–310.

796   Mørk, M.B.E., 1986. Coronite and eclogite formation in olivine gabbro (Western

797   Norway): reaction paths and garnet zoning. *Mineralogical Magazine*, **50**, no.

798   September.

799   Müller, S., 2013. Detailed study on microstructures and element mobility during fluid-

800   mediated pseudomorphic gabbro-to-eclogite transformation.

801   Nock, R. & Nielsen, F., 2004. Statistical Region Merging. *IEEE transactions on Pattern*

802   *Analysis and Machine Intelligence*, **26**, 1452–1458.

803   Padrón-Navarta, J.A., Garrido, C.J., Sánchez-Navas, A., Tommasi, A., Sánchez-

804   Vizcaíno, V.L., Gómez-Pugnaire, M.T. & Hussain, S.S., 2008. Oriented growth of

805   garnet by topotactic reactions and epitaxy in high-pressure, mafic garnet granulite

806   formed by dehydration melting of metastable hornblende-gabbronorite (Jijal

807   Complex, Kohistan Complex, north Pakistan). *Journal of Metamorphic Geology*,

808   **26**, 855–870.

809   Prior, D.J., Wheeler, J., Brenker, F.E., Harte, B. & Matthews, M., 2000. Crystal plasticity

810   of natural garnet: New microstructural evidence. *Geology*, **28**, 1003–1006.

811   Prior, D.J., Wheeler, J., Peruzzo, L., Spiess, R. & Storey, C., 2002. Some garnet

812   microstructures: An illustration of the potential of orientation maps and

813   misorientation analysis in microstructural studies. *Journal of Structural Geology*,

814   **24**, 999–1011.

815   Putnis, A. & Austrheim, H., 2010. Fluid-induced processes: metasomatism and

816   metamorphism. *Geofluids*, **10**, 254–269.

817   Putnis, A. & John, T., 2010. Replacement processes in the earth's crust. *Elements*, **6**,

818   159–164.

819   Rivers, M.L. & Wang, Y., 2006. Recent developments in microtomography at

820   GeoSoilEnviroCARS. *Proceedings of SPIE*, **6318**, 63180J–63180J–15.

821   Schindelin, J., Arganda-Carreras, I., Frise, E., Kaynig, V., Longair, M., Pietzsch, T.,

822   Preibisch, S., Rueden, C., Saalfeld, S., Schmid, B., Tinevez, J., White, D.J.,

823   Hartenstein, V., Eliceiri, K. *et al.*, 2012. Fiji: an open-source platform for

824   biological-image analysis. *Nature Methods*, **9**, 676–682.

825   Schlüter, S., Sheppard, A., Brown, K. & Wildenschild, D., 2014. Image processing of

826   multiphase images obtained via X-ray microtomography: A review. *Water*

827   *Resources Research*, **50**, 3615–3639.

828   Smit, M., Scherer, E.E., John, T. & Janssen, A., 2011. Creep of garnet in eclogite:

829   Mechanisms and implications. *Earth and Planetary Science Letters*, **311**, 411–419.

830   Spiess, R., Peruzzo, L., Prior, D.J. & Wheeler, J., 2001. Development of garnet

831   porphyroblasts by multiple nucleation, coalescence and boundary driven rotations.

832   *Journal of Metamorphic Geology*, **19**, 269–290.

833   Storey, C.D. & Prior, D.J., 2005. Plastic deformation and recrystallization of garnet: A

834   mechanism to facilitate diffusion creep. *Journal of Petrology*, **46**, 2593–2613.

835   Terry, M.P. & Heidelbach, F., 2006. Deformation-enhanced metamorphic reactions and

836   the rheology of high-pressure shear zones, Western Gneiss Region, Norway.

837   *Journal of Metamorphic Geology*, **24**, 3–18.

838   Terry, M.P. & Heidelbach, F., 2004. Superplasticity in garnet from eclogite facies shear

839   zones in the Haram Gabbro, Haramsøya, Norway. *Geology*, **32**, 281.

840   Trepmann, C.A. & Stöckhert, B., 2002. Cataclastic deformation of garnet: A record of

841   synseismic loading and postseismic creep. *Journal of Structural Geology*, **24**, 1845–

842   1856.

843   Tschumperle, D. & Deriche, R., 2005. Vector-Valued Image Regularization with PDEs :

844   A Common Framework for Different Applications. *IEEE transactions on Pattern*

845   *Analysis and Machine Intelligence*, **27**, 506–517.

846   Viegas, G., Menegon, L. & Archanjo, C., 2016. Brittle grain-size reduction of feldspar,

847   phase mixing and strain localization in granitoids at mid-crustal conditions

848   (Pernambuco shear zone, NE Brazil). *Solid Earth*, **7**, 375–396.

849   Voegelé, V., Ando, J.I., Cordier, P. & Liebermann, R.C., 1998. Plastic deformation of

850   silicate garnets. I. High-pressure experiments. *Physics of the Earth and Planetary*

851   *Interiors*, **108**, 305–318.

852   Wain, A., Waters, D.J. & Austrheim, H., 2001. Metastability of granulites and processes

853   of eclogitisation in the UHP region of western Norway. *Journal of Metamorphic*

854   *Geology*, **19**, 609–625.

855   Wang, Z. & Ji, S., 1999. Deformation of silicate garnets: Brittle-ductile transition and its

856   geological implications. *Canadian Mineralogist*, **37**, 525–541.

857   Wayte, G.J., Worden, R.H., Rubie, D.C. & Droop, G.T.R., 1989. A TEM study of

858   disequilibrium plagioclase breakdown at high pressure: the role of infiltrating fluid.

859   *Contributions to Mineralogy and Petrology*, **101**, 426–437.

860   Whitney, D.L., Goergen, E.T., Ketcham, R. A. & Kunze, K., 2008. Formation of garnet

861   polycrystals during metamorphic crystallization. *Journal of Metamorphic Geology*,

862   **26**, 365–383.

863   Whitney, D.L. & Seaton, N.C.A., 2010. Garnet polycrystals and the significance of

864   clustered crystallization. *Contributions to Mineralogy and Petrology*, **160**, 591–607.

865   Zhang, J. & Green, H.W., 2007. Experimental investigation of eclogite rheology and its

866   fabrics at high temperature and pressure. *Journal of Metamorphic Geology*, **25**, 97–

867   115.

868 **SUPPORTING INFORMATION**

869 **Appendix S1 Ground-truthing: Correlating synchroton x-ray micro-tomography**

870 **data with chemical compositions**

871 **Appendix S2 Segmentation of micro-tomographic data**

872 **Appendix S3 4D evolution of grain shapes**

873 **Fig. S1** Grey value histograms calculated from three SµCT datasets. The calculated

874 absorption coefficients (µ) for the mineral phases correlate with grey scale values

875 measured on the microtomographic data. The histograms reflect the metamorphic

876 reactions during strain localization.

877 **Fig. S2** Schematic workflow used to analyse the microtomographic data.

878 **Fig. S3** EBSD results of low strain domain (sample 066B2). On EBSD-derived maps,

879 high-angle boundaries (grain boundaries, misorientation > 10°) and low-angle boundaries

880 (subgrain boundaries, misorientation > 3° and < 10°) were indicated with black and

881 fuchsia lines, respectively. A) Phase map: Olivine (yellow), Plagioclase (white),

882 Orthopyroxene (blue), Garnet (red), Hornblende (green). Red lines represent twinning

883 boundaries in plagioclase. B) Inverse Pole Figure of Garnet in relation to the stretching

884 lineation in the shear zone. Legend on bottom left corner. C) Local Misorientation Map,

885 and legend, representing local misorientations from 0 (blue) to 9 degrees misorientation

886 (red). The arrow indicates the average local internal misorientation. D) Misorientation

887 profile A-A', location shown in figure C.

888 **Fig. S4** EBSD results of low strain domain (sample 066B2). E) Pole figures of garnet. F)

889 Pole figure of hornblende. G) Misorientation axis in crystal coordinates for low angle

890   boundaries (3-10°).

891   **Fig. S5** EBSD results of intermediate strain domain (sample 0617). A) Inverse Pole

892   Figure of garnet. Legend as in Fig. S3B. B) Local Misorientation Map, and legend

893   representing local misorientations from 0 (blue) to 9 degrees misorientation (red). The

894   arrow indicates the average local internal misorientation. C) Misorientation profile A-A',

895   location is shown in figure A. D) Misorientation profile B-B', location shown in figure

896   A. E) Pole figures of garnet. The trace of the shear foliation is oriented NW-SE, pole

897   figures are oriented with the trace of the mylonitic foliation parallel to the diameter (E-

898   W). F) Misorientation axis of low angle boundaries (3-10°) in crystal coordinates.

899   **Fig. S6** EBSD results of high strain domain (sample 0618). A) Phase map: Grt (red), Am

900   (green), Opx (blue), Bt (yellow). B) Local Misorientation Map, and legend representing

901   local misorientations from 0 (blue) to 9 degrees misorientation (red). The arrow indicates

902   the average local internal misorientation. C) Inverse Pole Figure of garnet. Legend as in

903   Fig. S3B. D) Misorientation profile A-A', location is shown in figure C. E)

904   Misorientation profile B-B', location shown in figure C. F) Misorientation profile C-C',

905   location shown in figure C.

906   **Fig. S7** EBSD results of high strain domain (sample 0618). A) Pole figures of garnet.

907   The trace of the shear foliation is oriented NNE-SSW, pole figures are oriented with the

908   trace of the mylonitic foliation parallel to the diameter (E-W). B) Pole figures of

909   hornblende. C) Misorientation axis of low angle boundaries (3-10°) in crystal

910   coordinates.

911   **Fig. S8** The image shows the results of Statistical Region Merging technique for

41

912   increasing Q. Scale as in image A. A) Original data. B) SRM Q=2. C) SRM Q=10. D)

913   SRM Q=25: note that the image is more detailed. E, F, G) Histograms relative to the

914   three different SRM parameters.

915   **Fig. S9** Outputs of segmentation for olivine (green) and garnet (blue) grains, in the low

916   strain domain (different viewing angles). The red arrows indicate olivine grains that are

917   not completely enclosed by garnet coronas.

918   **Fig. S10** Label analysis of intermediate strain domain after erosion. The large

919   interconnected voxel cluster is now divided in disconnected subvoxel clusters. Long

920   side 2630 µm.

921   **Fig. S11** Quant3D explained. The tomographic data are first segmented to extrapolate

922   the material of interest. Star points are placed within the segmented material: the

923   distance of each star points to the next material boundary are calculated in many

924   orientations and normalised. Simplified from Ketcham (2005).

925   **Fig. S12** Results of Quant3D analysis on eroded data, from low strain (A) to high strain

926   (C). With increasing deformation, garnet grains evolve from isodiametric shapes to

927   more progressively discoid shapes as a results of the deformation.

928   **Table S1** Electron microprobe chemical compositions of oxides in garnets, used to

929   calculate the x-ray absorption coefficients.

930   **Table S2** Representative garnet structural formulae for the low (#066B2) and high

931   (#0618) strain domain obtained from the microprobe analyses at the University of

932   Münster.

933   **Table S3** Frequency distribution data for non-eroded data. The first column of each

934   dataset refers to absolute frequency, the second one to the cumulative frequency relative

935   to the total amount of garnet in each sample.

936   **Table S4** Frequency distribution data for eroded data. Bins refer to cubic micrometres.

937   The first column of each dataset refers to absolute frequency, the second one to the

938   cumulative frequency relative to the total amount of garnet in each sample.

939

940

941

942   **FIGURE CAPTIONS**

943   **Fig. 1** The illustration shows the approximate original position (circles) of thin sections

944   in the hand specimen, and the positions of tomographic data in the thin sections which

945   are indicated by the red squares. 3D volume renderings, derived from tomographic data

946   from the three samples, are shown in the bottom part. Slice is cut parallel to the fabric

947   attractor. Axis for the kinematic frame (X, Y, Z) are indicated in the microtomographic

948   data.

949   **Fig. 2** Microtomographic datasets: A) low strain, B) intermediate strain, and C) high

950   strain. Figure A exhibits minor artefacts (horizontal stripes) that do not affect the

951   analyses. Mineral phases and features are recognizable from the corresponding SEM

952   images (Fig. 3). The images represent the XZ plane and are parallel to the thin sections.

953   **Fig. 3** BSE images of Krakeneset samples and corresponding microtomographic

954   datasets, from low to high strain domain respectively: A) Sample 066B2 (Low strain)-

955   Olivine grains are surrounded by complex coronas of orthopyroxene, garnet and

956   amphibole. B) 3-dimensional dataset of low strain domain: high-pressure amphibole-

957   garnet coronas surround olivine grains (dimensions 1503 x 1196 x 1831 cubic voxels).

958   Note the variable thickness of amphibole. C) Sample 0617 (Intermediate Strain)- In the

959   intermediate strain domain, olivine cores are replaced by orthopyroxene, while garnet

960   and amphibole are no more part of the corona structures. D) Corresponding

961   microtomographic dataset (dimensions 1322 x 1219 x 2023 cubic voxels). E) Sample

962   0618 (High Strain)- The high strain domain is characterized by a compositional layering

963   of elongated garnet and plagioclase versus orthopyroxene and amphibole rich layers. F)

44

964   Microtomographic dataset of the high strain domain (dimensions 1313 x 1234 x 1980

965   cubic voxels): note garnet grains behaving as rigid objects in a more ductile matrix of

966   orthopyroxene and amphibole.

967   **Fig. 4** A) Optical microscope image illustrating the mineral phases and microstructures

968   present in the more deformed samples. B) BSE image showing old olivine cores now

969   replaced by orthopyroxene-amphibole symplectites. Relict cores of magmatic

970   clynopyroxene are present (Mag_Cpx "relict"), and are surrounded by a thin rim of

971   omphacite (Omp), which is present also between garnet and orthopyroxene-amphibole

972   symplectites ("Opx-Amp Symp"). C) Symplectites of albite-clinozoisite are replacing the

973   plagioclase; omphacite surrounds relict magmatic clynopyroxene (Mag_Cpx "relict")

974   and orthopyroxene-amphibole symplectites.

975   **Fig. 5** Grs-Alm-Py plot showing garnet compositions from EMPA analyses, as single

976   measurements across different grains. Filled symbols represent compositions closer to

977   the plagioclase source. Empty symbols represent compositions closer to Fe-Mg-rich

978   phases. End-members values are presented in the graph by the large symbols. With

979   increasing deformation, garnet compositions become more Alm-rich, a trend expected

980   for a gabbro that is equilibrating under P-T-t conditions of eclogite facies. In Tab. S2,

981   representative structural formulae are reported for the three samples.

982   **Fig. 6** Compositional maps for CaO and MgO for the low (A-C) and high (B-D) strain

983   domains, obtained using XMapTools v. 2.3.1 (Lanari *et al.*, 2014). CaO and MgO do

984   have the same compositional zoning (4-10%) in the most deformed sample. C) Many

985   garnets in the high strain domain have low CaO, reflecting an equilibration towards Alm-

986   rich compositions. Nevertheless, some grain do have a higher content in CaO (~10%)

45

987   (a') and MgO (~11%) (b'): we interpret this to results from coalescence (a, b) and

988   subsequent disintegration of individual zoned coronas. Further left in Figure C, garnets

989   are fragmented and forming a fine-grained matrix, indicating collapse of an old pre-

990   existing corona.

991   **Fig. 7** The figures illustrate the results of segmentation of garnet from the

992   microtomographic data. Top: cropped volumes of original datasets (~0.5 mm^3); bottom:

993   garnets rendered in purple. Fog is added within the datasets to better visualize the 3D

994   architecture. A) Low strain, B) Intermediate strain, C) High strain. Note 3D orientation

995   and texture of garnet grains. Note the presence of more faceted grains in the intermediate

996   and high strain domain.

997   **Fig. 8** Garnet voxel cluster size distribution for non-eroded (solid lines) and eroded

998   (dashed lines) data. From low to high strain, there is an increase in frequency for all size

999   classes with increasing strain. Note the presence of the very large interconnected garnet

1000   voxel cluster in the low strain domain (blue solid curve), while the presence of much

1001   smaller sizes in the most deformed sample. The sketch on the top left corner illustrates

1002   the erosion process and the effects of particle size and shape: some particle might

1003   completely disappear. A, B) Absolute frequency and cumulative volume, respectively,

1004   for the low strain sample. C, D) Absolute frequency and cumulative volume,

1005   respectively, for the intermediate strain sample. E, F) Absolute frequency and cumulative

1006   volume, respectively, for the high strain sample.

1007   **Fig. 9** Label analysis of the end-members of the studied samples. A) 3D volume

1008   rendering of labels relative to low strain domain (dimensions 1503 x 1196 x 1831 cubic

46

1009   voxels). B) Intermediate Strain (dimensions 1322 x 1219 x 2023 cubic voxels). C) High

1010   strain (dimensions 1313 x 1234 x 1980 cubic voxels). Individual disconnected

1011   aggregates of garnet are identified with different colours.

1012   **Fig. 10** EBSD analysis results. Low strain: A) IPF map superposed on a pattern quality

1013   (Band Contrast) map. B) Profile X-Y, location in figure A). C) Misorientation axis by

1014   crystal coordinates for low angle boundaries (3-10°). Intermediate strain domain: D)

1015   IPF map. E) Profile X-Y, location in figure D; F) Misorientation axis by crystal

1016   coordinates for low angle boundaries (3-10°). High strain: G) IPF map. H) Profile X-Y,

1017   location in figure G; I) Misorientation axis by crystal coordinates for low angle

1018   boundaries (3-10°).

1019   **Fig. 11** Schematic sketch illustrating the evolution of reaction microfabrics, and in

1020   particular of garnet grains. 1) Low strain domain. 2) Intermediate strain. 3) High strain.

1021   See text for discussion.
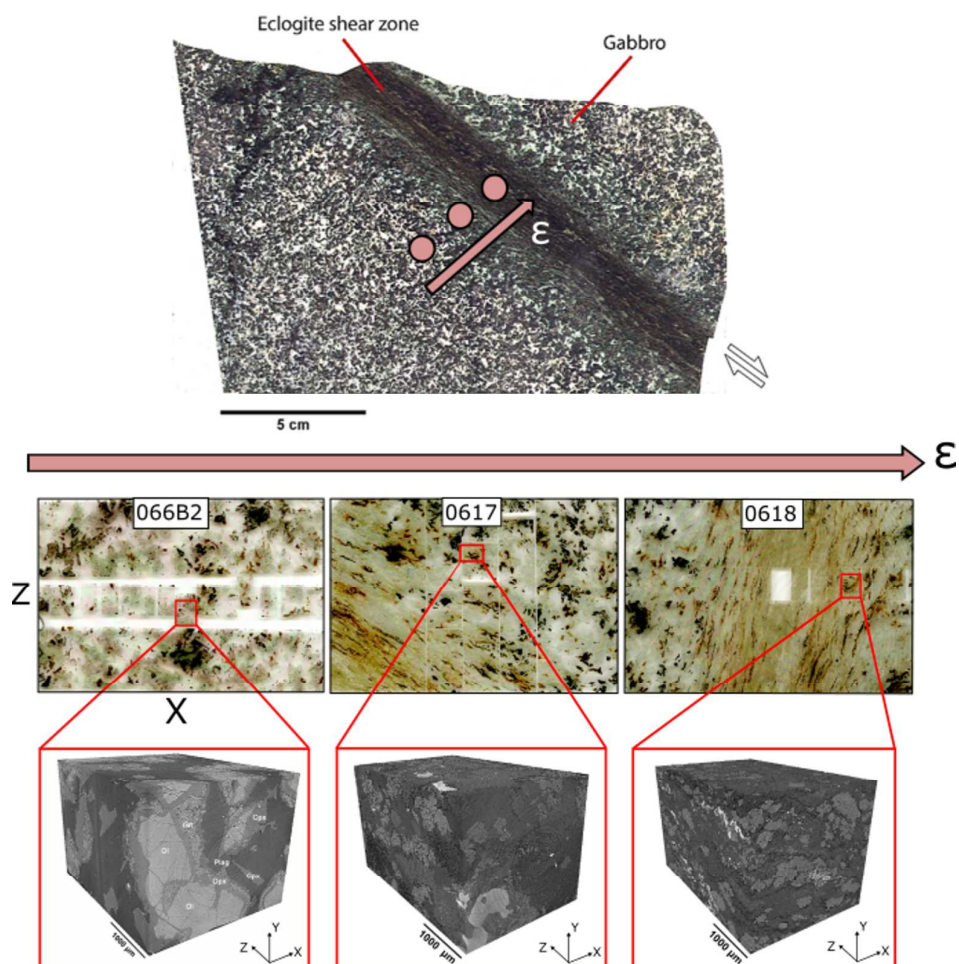
Fig. 1 The illustration shows the approximate original position (circles) of thin sections in the hand specimen, and the positions of tomographic data in the thin sections which are indicated by the red squares. 3D volume renderings, derived from tomographic data from the three samples, are shown in the bottom part. Slice is cut parallel to the fabric attractor. Axis for the kinematic frame (X, Y, Z) are indicated in the microtomographic data.

150x152mm (300 x 300 DPI)
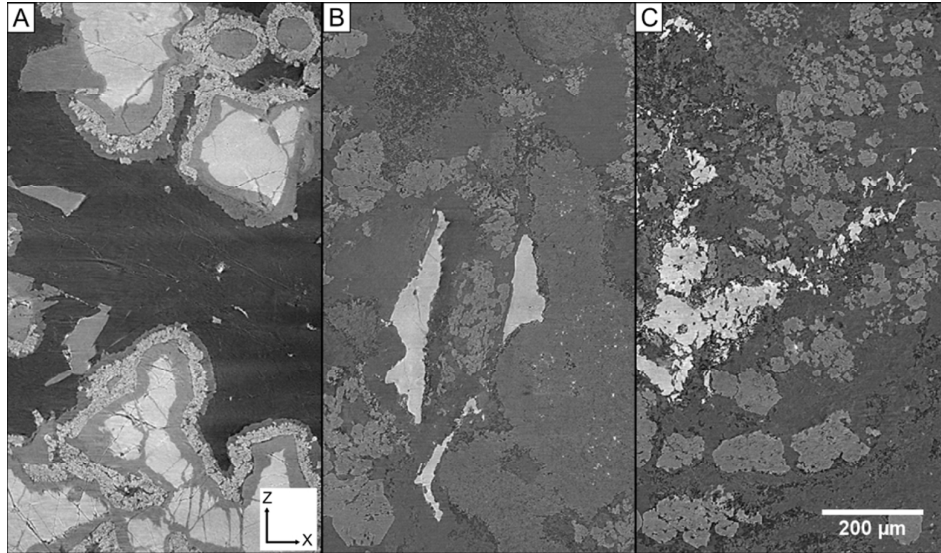
Fig. 2 Microtomographic datasets: A) low strain, B) intermediate strain, and C) high strain. Figure A exhibits minor artefacts (horizontal stripes) that do not affect the analyses. Mineral phases and features are recognizable from the corresponding SEM images (Fig. 3). The images represent the XZ plane and are parallel to the thin sections.

150x87mm (300 x 300 DPI)
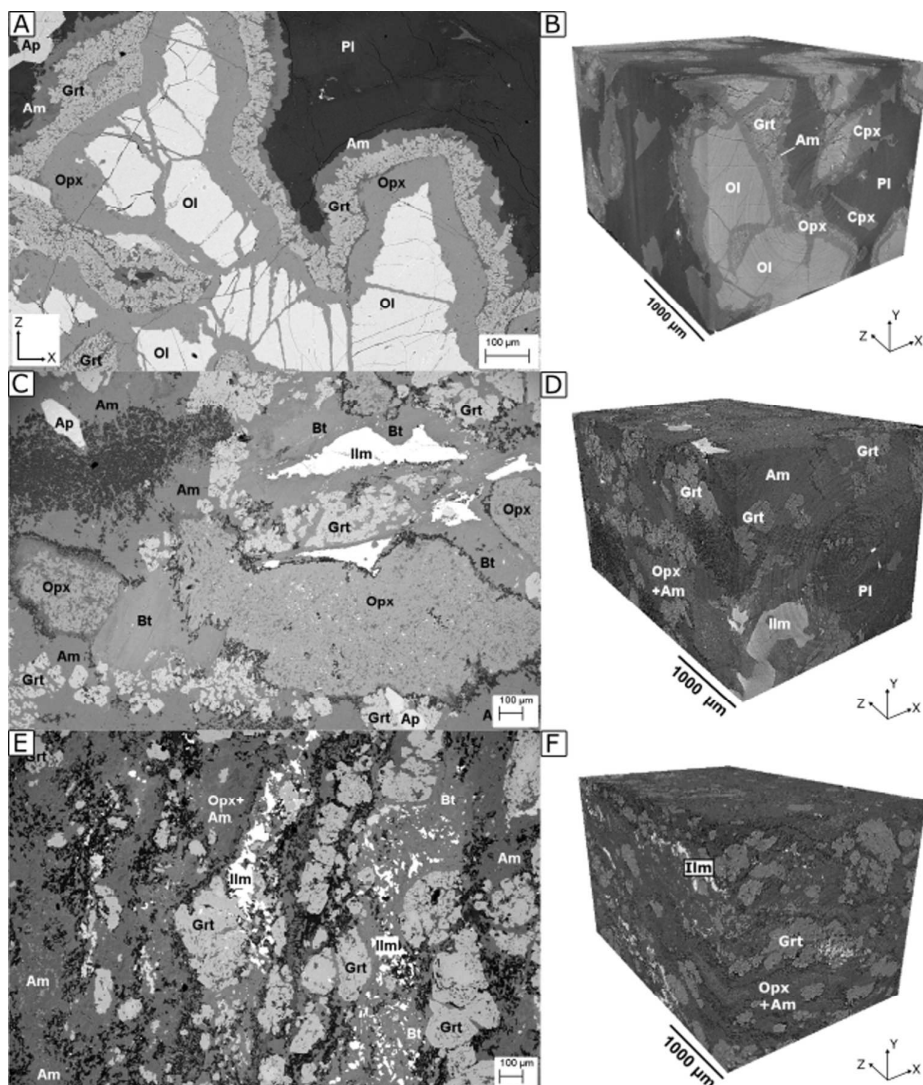
Fig. 3 BSE images of Krakeneset samples and corresponding microtomographic datasets, from low to high strain domain respectively: A) Sample 066B2 (Low strain)- Olivine grains are surrounded by complex coronas of orthopyroxene, garnet and amphibole. B) 3-dimensional dataset of low strain domain: high-pressure amphibole-garnet coronas surround olivine grains (dimensions 1503 x 1196 x 1831 cubic voxels). Note the variable thickness of amphibole. C) Sample 0617 (Intermediate Strain)- In the intermediate strain domain, olivine cores are replaced by orthopyroxene, while garnet and amphibole are no more part of the corona structures. D) Corresponding microtomographic dataset (dimensions 1322 x 1219 x 2023 cubic voxels). E) Sample 0618 (High Strain)- The high strain domain is characterized by a compositional layering of elongated garnet and plagioclase versus orthopyroxene and amphibole rich layers. F) Microtomographic dataset of the high strain domain (dimensions 1313 x 1234 x 1980 cubic voxels): note garnet grains behaving as rigid objects in a more ductile matrix of orthopyroxene and amphibole.

150x171mm (300 x 300 DPI)
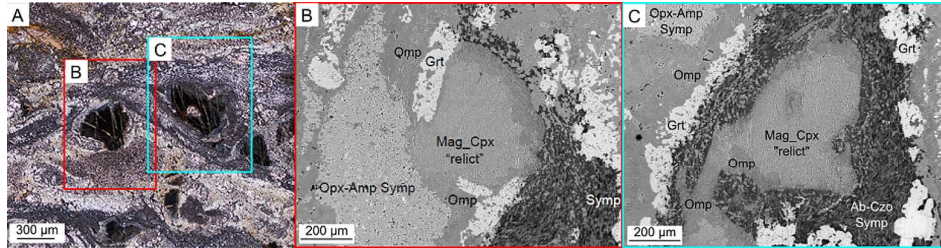
Fig. 4 A) Optical microscope image illustrating the mineral phases and microstructures present in the more deformed samples. B) BSE image showing old olivine cores now replaced by orthopyroxene-amphibole symplectites. Relict cores of magmatic clynopyroxene are present (Mag_Cpx "relict"), and are surrounded by a thin rim of omphacite (Omp), which is present also between garnet and orthopyroxene-amphibole symplectites ("Opx-Amp Symp"). C) Symplectites of albite-clinozoisite are replacing the plagioclase; omphacite surrounds relict magmatic clynopyroxene (Mag_Cpx "relict") and orthopyroxene-amphibole symplectites.

150x39mm (300 x 300 DPI)
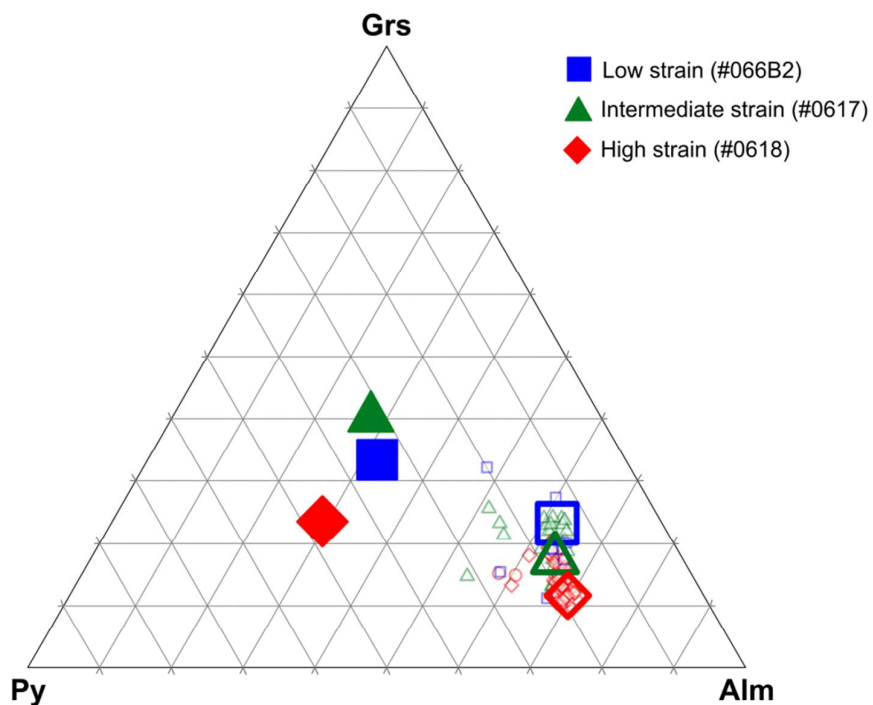
Fig. 5 Grs-Alm-Py plot showing garnet compositions from EMPA analyses, as single measurements across different grains. Filled symbols represent compositions closer to the plagioclase source. Empty symbols represent compositions closer to Fe-Mg-rich phases. End-members values are presented in the graph by the large symbols. With increasing deformation, garnet compositions become more Alm-rich, a trend expected for a gabbro that is equilibrating under P-T-t conditions of eclogite facies. In Tab. S2, representative structural formulae are reported for the three samples.

99x75mm (300 x 300 DPI)
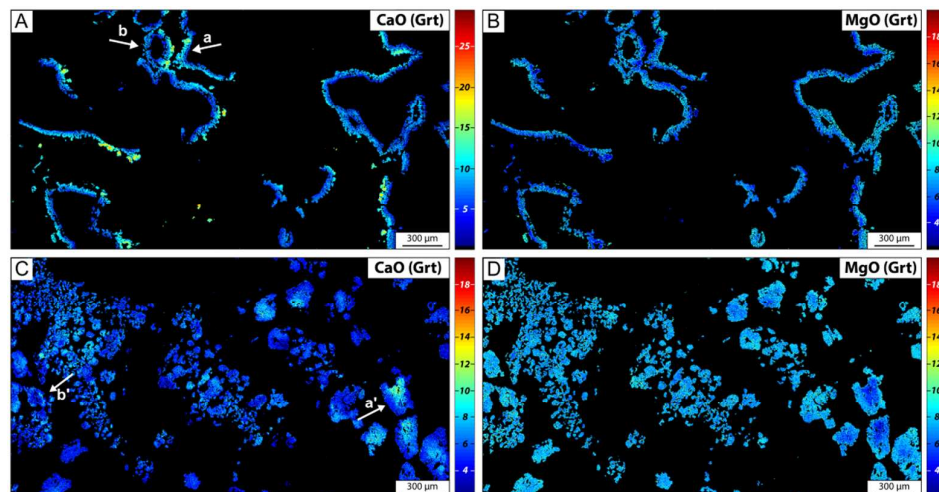
Fig. 6 Compositional maps for CaO and MgO for the low (A-C) and high (B-D) strain domains, obtained using XMapTools v. 2.3.1 (Lanari et al., 2014). CaO and MgO do have the same compositional zoning (4-10%) in the most deformed sample. C) Many garnets in the high strain domain have low CaO, reflecting an equilibration towards Alm-rich compositions. Nevertheless, some grain do have a higher content in CaO (~10%) (a') and MgO (~11%) (b'): we interpret this to results from coalescence (a, b) and subsequent disintegration of individual zoned coronas. Further left in Figure C, garnets are fragmented and forming a fine-grained matrix, indicating collapse of an old pre-existing corona.

150x78mm (300 x 300 DPI)
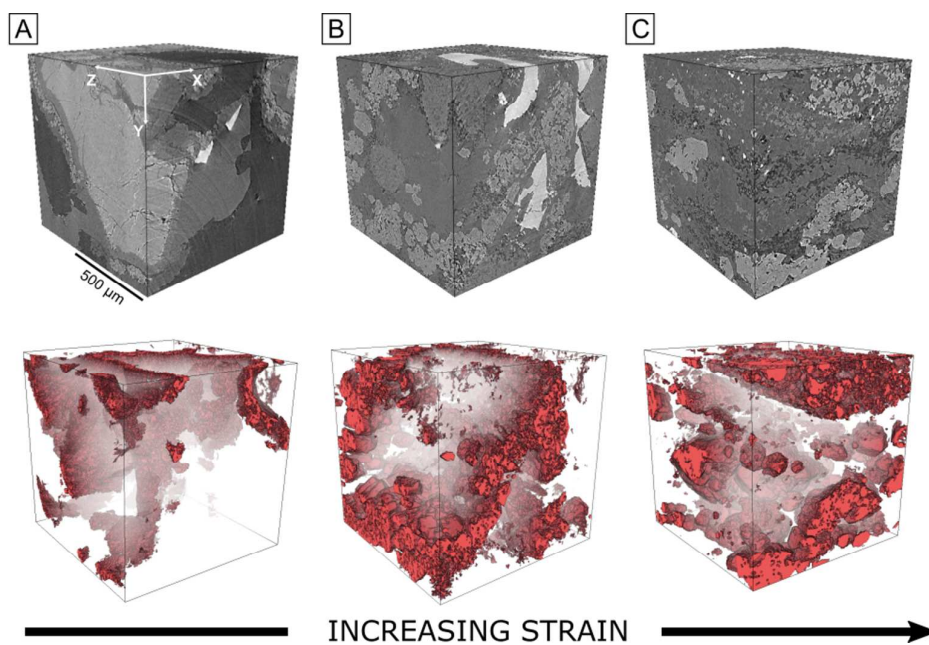
Fig. 7 The figures illustrate the results of segmentation of garnet from the microtomographic data. Top: cropped volumes of original datasets (~0.5 mm3); bottom: garnets rendered in purple. Fog is added within the datasets to better visualize the 3D architecture. A) Low strain, B) Intermediate strain, C) High strain. Note 3D orientation and texture of garnet grains. Note the presence of more faceted grains in the intermediate and high strain domain.
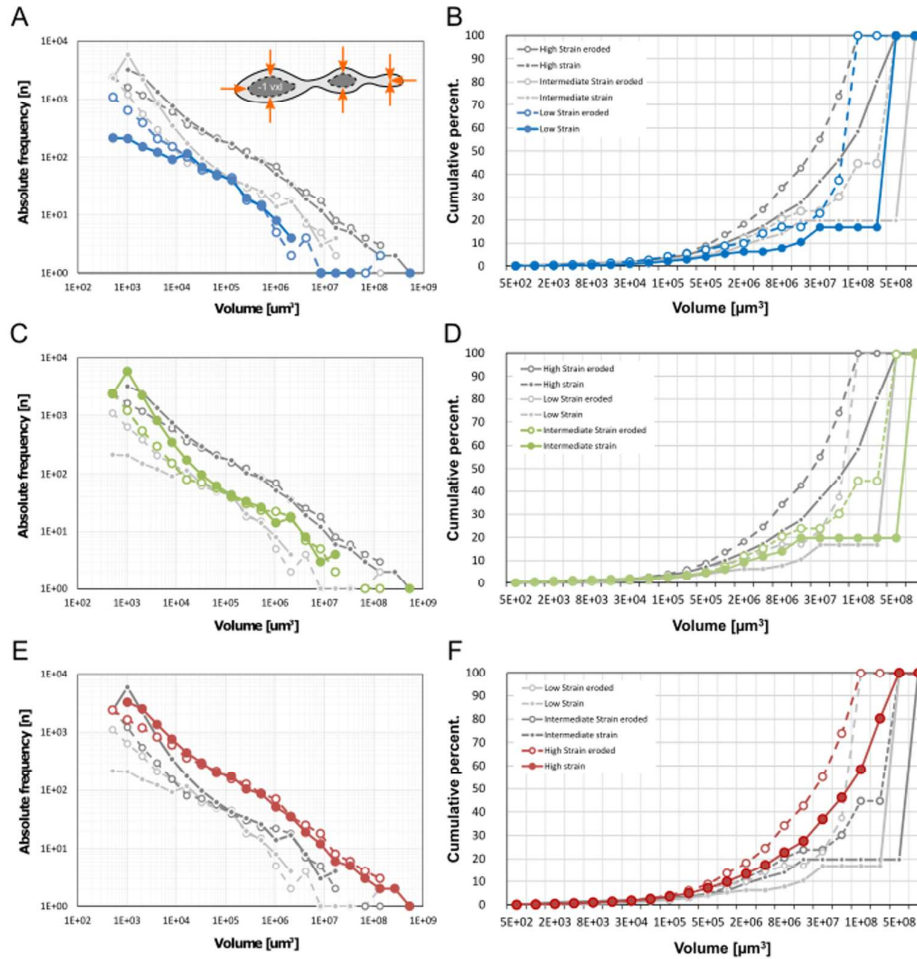
140x93mm (300 x 300 DPI)

Fig. 8 Garnet voxel cluster size distribution for non-eroded (solid lines) and eroded (dashed lines) data. From low to high strain, there is an increase in frequency for all size classes with increasing strain. Note the presence of the very large interconnected garnet voxel cluster in the low strain domain (blue solid curve), while the presence of much smaller sizes in the most deformed sample. The sketch on the top left corner illustrates the erosion process and the effects of particle size and shape: some particle might completely disappear. A, B) Absolute frequency and cumulative volume, respectively, for the low strain sample. C, D) Absolute frequency and cumulative volume, respectively, for the intermediate strain sample. E, F) Absolute frequency and cumulative volume, respectively, for the high strain sample.
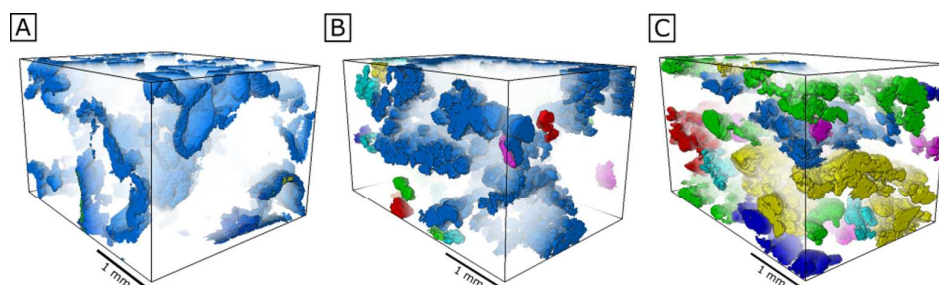
140x141mm (300 x 300 DPI)

Fig. 9 Label analysis of the end-members of the studied samples. A) 3D volume rendering of labels relative to low strain domain (dimensions 1503 x 1196 x 1831 cubic voxels). B) Intermediate Strain (dimensions 1322 x 1219 x 2023 cubic voxels). C) High strain (dimensions 1313 x 1234 x 1980 cubic voxels). Individual disconnected aggregates of garnet are identified with different colours.
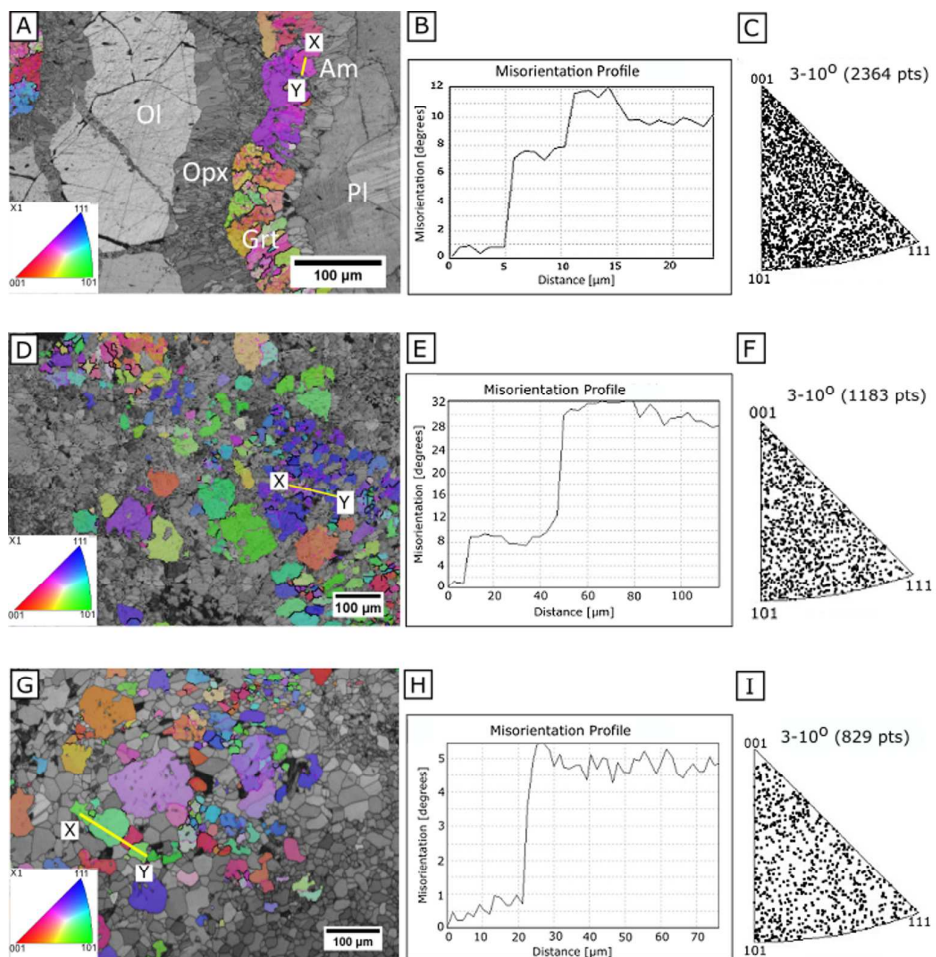
150x44mm (300 x 300 DPI)

Fig. 10 EBSD analysis results. Low strain: A) IPF map superposed on a pattern quality (Band Contrast) map. B) Profile X-Y, location in figure A). C) Misorientation axis by crystal coordinates for low angle boundaries (3-10°). Intermediate strain domain: D) IPF map. E) Profile X-Y, location in figure D; F) Misorientation axis by crystal coordinates for low angle boundaries (3-10°). High strain: G) IPF map. H) Profile X-Y, location in figure G; I) Misorientation axis by crystal coordinates for low angle boundaries (3-10°).
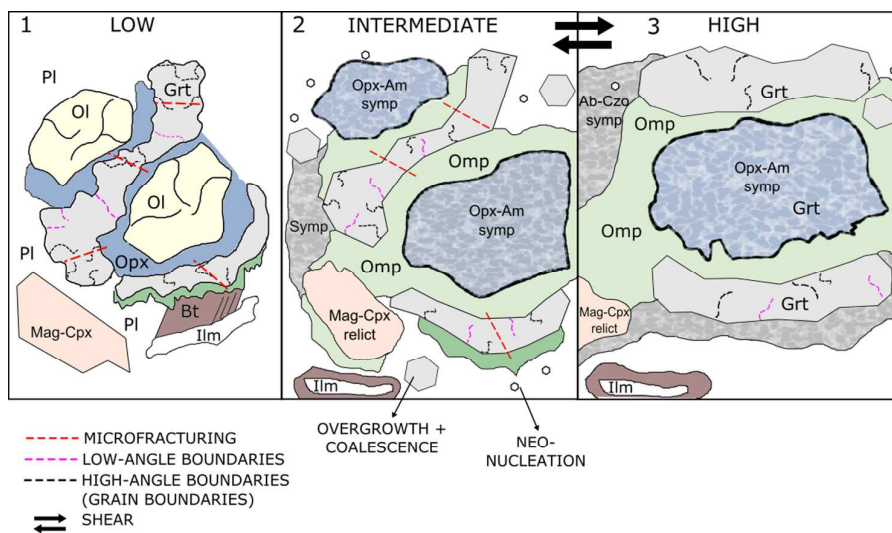
150x151mm (300 x 300 DPI)

Fig. 11 Schematic sketch illustrating the evolution of reaction microfabrics, and in particular of garnet grains. 1) Low strain domain. 2) Intermediate strain. 3) High strain. See text for discussion.

150x82mm (300 x 300 DPI)

SUPPORTING INFORMATION

The strain-dependent evolution of garnet in a high-pressure ductile shear zone from the Western Gneiss Region (Norway): a Synchrotron x-ray microtomography study

Alice Macente*****, Florian Fusseis, Luca Menegon, Xianghui Xiao, Timm John

*email: alice.macente@ed.ac.uk

Appendix S1 Ground-truthing: Correlating synchroton x-ray micro-tomography data with chemical compositions

Appendix S2 Segmentation of micro-tomographic data

Appendix S3 4D evolution of grain shapes

Fig. S1 Grey value histograms calculated from three SµCT datasets. The calculated absorption coefficients (µ) for the mineral phases correlate with grey scale values measured on the microtomographic data. The histograms reflect the metamorphic reactions during strain localization.

Fig. S2 Schematic workflow used to analyse the microtomographic data.

Fig. S3 EBSD results of low strain domain (sample 066B2). On EBSD-derived maps, high-angle boundaries (grain boundaries, misorientation > 10°) and low-angle boundaries (subgrain boundaries, misorientation > 3° and < 10°) were indicated with black and fuchsia lines, respectively. A) Phase map: Olivine (yellow), Plagioclase (white), Orthopyroxene (blue), Garnet (red), Hornblende (green). Red lines represent twinning boundaries in plagioclase. B) Inverse Pole Figure of Garnet in relation to the stretching lineation in the shear zone. Legend on bottom left corner. C) Local Misorientation Map, and legend, representing local misorientations from 0 (blue) to 9 degrees misorientation (red). The arrow indicates the average local internal misorientation. D) Misorientation profile A-A', location shown in figure C.

Fig. S4 EBSD results of low strain domain (sample 066B2). E) Pole figures of garnet. F) Pole figure of hornblende. G) Misorientation axis in crystal coordinates for low angle boundaries (3-10°).

Fig. S5 EBSD results of intermediate strain domain (sample 0617). A) Inverse Pole Figure of garnet. Legend as in Fig. S3B. B) Local Misorientation Map, and legend representing local misorientations from 0 (blue) to 9 degrees misorientation (red). The arrow indicates the average local internal misorientation. C) Misorientation profile A-A', location is shown in figure A. D) Misorientation profile B-B', location shown in figure A. E) Pole figures of garnet. The trace of the shear foliation is oriented NW-SE, pole figures are oriented with the trace of the mylonitic foliation parallel to the diameter (E-W). F) Misorientation axis of low angle boundaries (3-10°) in crystal coordinates.

Fig. S6 EBSD results of high strain domain (sample 0618). A) Phase map: Grt (red), Am (green), Opx (blue), Bt (yellow). B) Local Misorientation Map, and legend representing local misorientations from 0 (blue) to 9 degrees misorientation (red). The arrow indicates the average local internal misorientation. C) Inverse Pole Figure of garnet. Legend as in Fig. S3B. D) Misorientation profile A-A', location is shown in figure C. E) Misorientation profile B-B', location shown in figure C. F) Misorientation profile C-C', location shown in figure C.

Fig. S7 EBSD results of high strain domain (sample 0618). A) Pole figures of garnet. The trace of the shear foliation is oriented NNE-SSW, pole figures are oriented with the trace of the mylonitic foliation parallel to the diameter (E-W). B) Pole figures of hornblende. C) Misorientation axis of low angle boundaries (3-10°) in crystal coordinates.

Fig. S8 The image shows the results of Statistical Region Merging technique for increasing Q. Scale as in image A. A) Original data. B) SRM Q=2. C) SRM Q=10. D) SRM Q=25: note that the image is more detailed. E, F, G) Histograms relative to the three different SRM parameters.

Fig. S9 Outputs of segmentation for olivine (green) and garnet (blue) grains, in the low

2

strain domain (different viewing angles). The red arrows indicate olivine grains that are not completely enclosed by garnet coronas.

Fig. S10 Label analysis of intermediate strain domain after erosion. The large interconnected voxel cluster is now divided in disconnected subvoxel clusters. Long side 2630 μm.

Fig. S11 Quant3D explained. The tomographic data are first segmented to extrapolate the material of interest. Star points are placed within the segmented material: the distance of each star points to the next material boundary are calculated in many orientations and normalised. Simplified from Ketcham (2005).

Fig. S12 Results of Quant3D analysis on eroded data, from low strain (A) to high strain (C). With increasing deformation, garnet grains evolve from isodiametric shapes to more progressively discoid shapes as a results of the deformation.

Table S1 Electron microprobe chemical compositions of oxides in garnets, used to calculate the x-ray absorption coefficients.

Table S2 Representative garnet structural formulae for the low (#066B2) and high (#0618) strain domain obtained from the microprobe analyses at the University of Münster.

Table S3 Frequency distribution data for non-eroded data. The first column of each dataset refers to absolute frequency, the second one to the cumulative frequency relative to the total amount of garnet in each sample.

Table S4 Frequency distribution data for eroded data. Bins refer to cubic micrometres. The first column of each dataset refers to absolute frequency, the second one to the cumulative frequency relative to the total amount of garnet in each sample.

Appendix S1 Ground-truthing: Correlating synchroton x-ray micro-tomography data with chemical compositions

Where x-ray microtomographic data allow for a complete visualisation of microfabrics in rocks in 3D (Denison and Carlson, 1997; Gualda and Rivers, 2006; Whitney et al., 2008; Wang et al., 2011; Goergen and Whitney, 2012; Sayab et al., 2014), the combination with established microanalytical techniques critically expands our insight into tectonic and metamorphic processes. High-resolution microtomographic data and electron microscopic analyses have similar resolutions on the μm-scale, and analytical results from the same samples can therefore be extrapolated between the techniques. The obvious gain from this is that metamorphic microfabrics can then be fully quantified in 3D. However, the marriage of 2D with 3D analyses hinges on a) a registration of the 2D data within the 3D dataset, b) a correlation of actual compositional data from the mineral phases with intensities recorded in the 3D scalar fields that make a microtomographic dataset (Gualda and Rivers, 2006) and c) the involved procedure of segmenting individual mineral volumes from the 3- dimensional datasets to allow for a further quantitative analysis. While routines for image registration are readily available, also in *AvizoFire*®, and segmentation is discussed in section 7.2, the following summarises our

3

strategy to correlate x-ray absorption with compositional information.

In most microtomographic data material-specific x-ray absorption is recorded as a function of position in the sample and, as an output of the reconstruction process, stored in an array of intensity values. The relationship between absorption and intensity (usually visualised as grey scale values) in the tomographic data is given by the Lambert-Beer law:

$$I = I_0 \exp\left[-\int_{-\infty}^{\infty} \mu(x)\,dx\right]$$

where I represents the intensity of the x-ray source before it hits the sample, I_0 is the attenuated intensity after x-rays passed through a sample of thickness x, and μ is a linear attenuation coefficient (e.g., Baker *et al.*, 2012; Fusseis *et al.*, 2014). The intensity distribution in a polymineralic sample can be plotted in a histogram that relates voxel frequency to recorded intensity (e.g., Fig. S1). Given that intensity is material-specific, these data can, in the best of cases, be used to quantify the volume of a particular mineral phase. However, it is important at this stage to establish a tight link between x-ray absorption microtomographic and actual compositional data from the same sample, and confirm that the grey values correspond to the minerals of interest. To achieve this we calculated the x-ray absorption coefficients for each mineral phase based on the chemical compositions acquired through EMPA analysis, and compared them with the grey scale distribution in the tomographic data (Fig. S1). X-ray mass attenuation coefficients are listed in a NIST (National Institute of Standards and Technology) database for elements Z=1 to 92, and for a number of substances of radiological interest. Where the energy of the incoming photons is known (in our case 27 KeV) and compositional data are available, the absorption coefficients can be calculated for any mineral. We used averaged electron microprobe analyses (EMPA) to calculate the theoretical x-ray mass attenuation coefficients of the minerals in our samples. Fig. S1 compares the calculated absorptions with three grey value histograms from the three studied datasets. Our analytical strategy, where the actual microtomography sample was polished and used for electron microscopy and EMPA analyses, allowed to combine compositional measurements with intensity signals and thereby anchor the two x-axes against each other. Fig. S1 does indeed capture some of the metamorphic processes that affect the samples. For example the peak for plagioclase, which is clearly present in the low strain dataset, is replaced by a minimum in the high strain domain, reflecting the lack (or a very small presence) of plagioclase in the eclogitic shear zone centre.

Appendix S2 Segmentation of micro-tomographic data

To be able to segment garnets from the tomographic images, we denoised the images in Fiji. The parameters for Anisotropic Diffusion Filter in 2D included 20 iterations, a_1 and a_2 were set up at 0.7 and 0.5 respectively. Before applying the filter, we improved the contrast on the images and saved them in Bitmap format in order to preserve the new contrast.

On the filtered data, Statistical Region Merging (SRM) technique was applied (Nock and Nielsen, 2004). This algorithm is a region growing technique, which groups

4

homogeneous pixels together and grow them iteratively together by merging other pixels or smaller regions. The limit of regions to be merged together is determined by a statistical test and the scale is controlled by the size of the parameter Q: the higher is Q, the higher is the number of subregions and the more detailed is the resulting image but it is also noisier (Nock and Nielsen, 2004) (Fig. S8). The changes operated by SRM can be visualised in the image histograms. Each boundary phase is marked in the histogram by a vertical bar, which allows *Global Threshold* to segment the material of interest in a more controlled way (Fig. S8). Global thresholding allows to select from the grey scale values in the histogram, and therefore from their x-ray absorption coefficient, a particular phase that can be extrapolated from the contest. In some cases, the choice of using one single output of SRM was insufficient. In Fiji, it was thus possible to combine different SRM outputs to obtain the best segmentation for garnet grains by using *Image Calculator* and the *Multiply* operator to get rid of unwanted segmented phases or islands.

A summary of the workflow used to analyse the data is shown in Figure S2.

Appendix S3 4D evolution of grain shapes

We performed Quant3D analysis to investigate the 3-dimensional shape of garnet grains and to understand if Synchroton x-ray micro-tomography can be used to gain information on the dynamic evolution of grain shapes. Quant3D is a fabric analysis software developed by Ketcham and Ryan (2004) and Ketcham (2005), written in IDL programming language and it includes three main fabric analysis methods. Originally developed by previous works for two-dimensional analysis (Ketcham (2005b) and references therein), these methods can now be used also to analyse 3-dimensional structures. The software gives the eigenvectors (û1, û2, û3) and eigenvalues (τ^1, τ^2, τ^3) of the fabric tensors, which define orthogonal principal axes and are related to the moment of inertia, the degree of anisotropies (*DA*), the isotropy index *I* and the elongation index (*E*) (Ketcham, 2005). The results can be visualized as a 3-dimensional rose diagram. In the rose diagram, each vertex is projected from the unit sphere either inward or outward from the origin of the star points. The vertex positions from the origin are normalized by the maximum distance value. In the rose diagram, eigenvectors, scaled by their respective eigenvalues, are also plotted. The rose diagram can be visualized as rendered surface with a colour code mode, where the red colour represents a normalized value of 1.0, as a distance from the origin equal to the coordinate axis length: lower values, indicating closer distances to the origin, are represented with cooler rainbow colours (Ketcham and Ryan (2004)). The results can be exported as VRML format, containing all the spatial information and readable by lots of applications. In our analysis, star points were placed outside the material of interest by assigning black values (0) to the garnets. In this way, the distances to the next material boundary represent distances to the material of interest, and thus they give an indication of the grain shapes. Analysis parameters were as followed: uniform distribution of orientations (513), random rotation, dense vectors. The results were exported as rose diagrams and VRML format files.

In order to avoid errors introduced by image segmentation, the analysis were performed on eroded data, as previously mentioned (subsection 4.3). The results are shown in Fig.

5

S12. With increasing strain, garnet shapes evolve from an isodiametric grain to increasingly discoidal and oblate shapes.
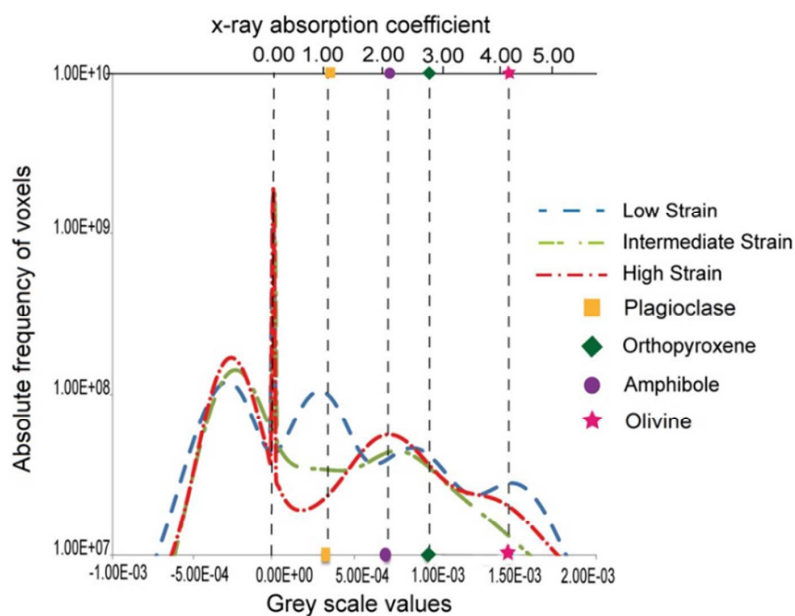
Fig. S1

Fig. S1 The graph shows grey value histograms calculated from three SμCT datasets. The calculated absorption coefficients (μ) for the mineral phases correlate with grey scale values measured on the microtomographic data. The histograms reflect the metamorphic reactions during strain localization.
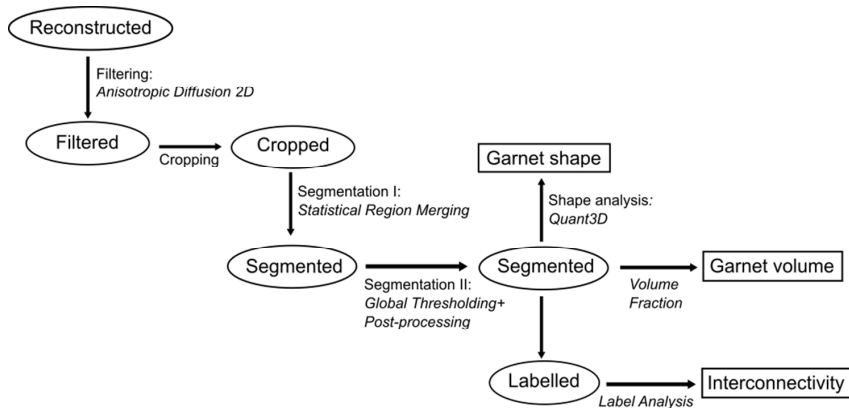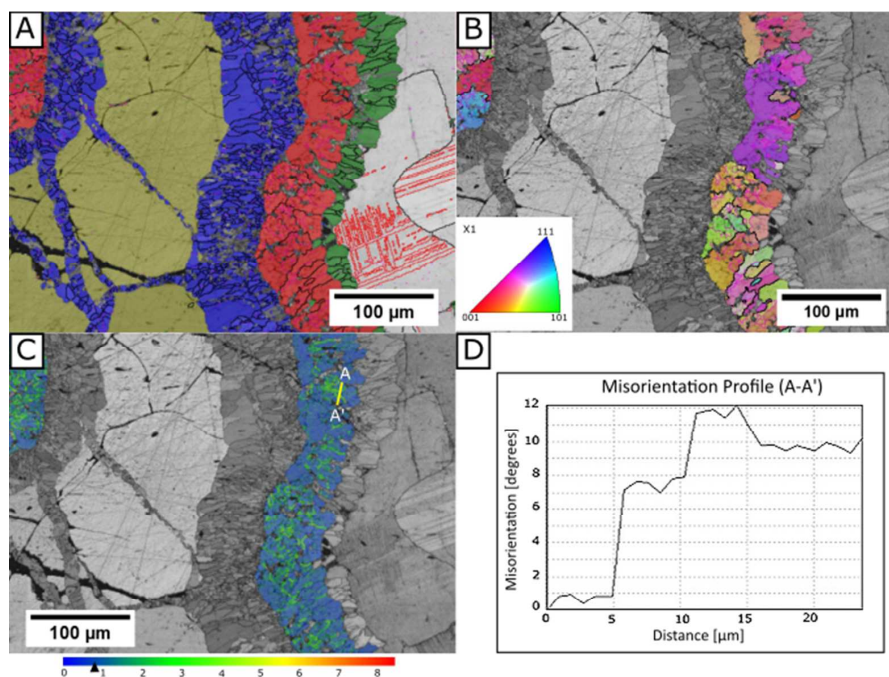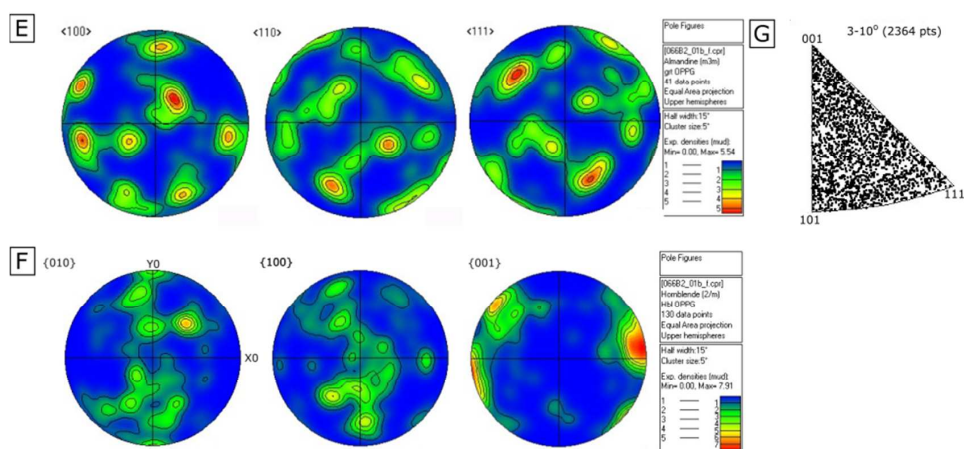
6

Fig. S2

Fig. S2 Schematic workflow used to analyse the microtomographic data.

Fig. S3
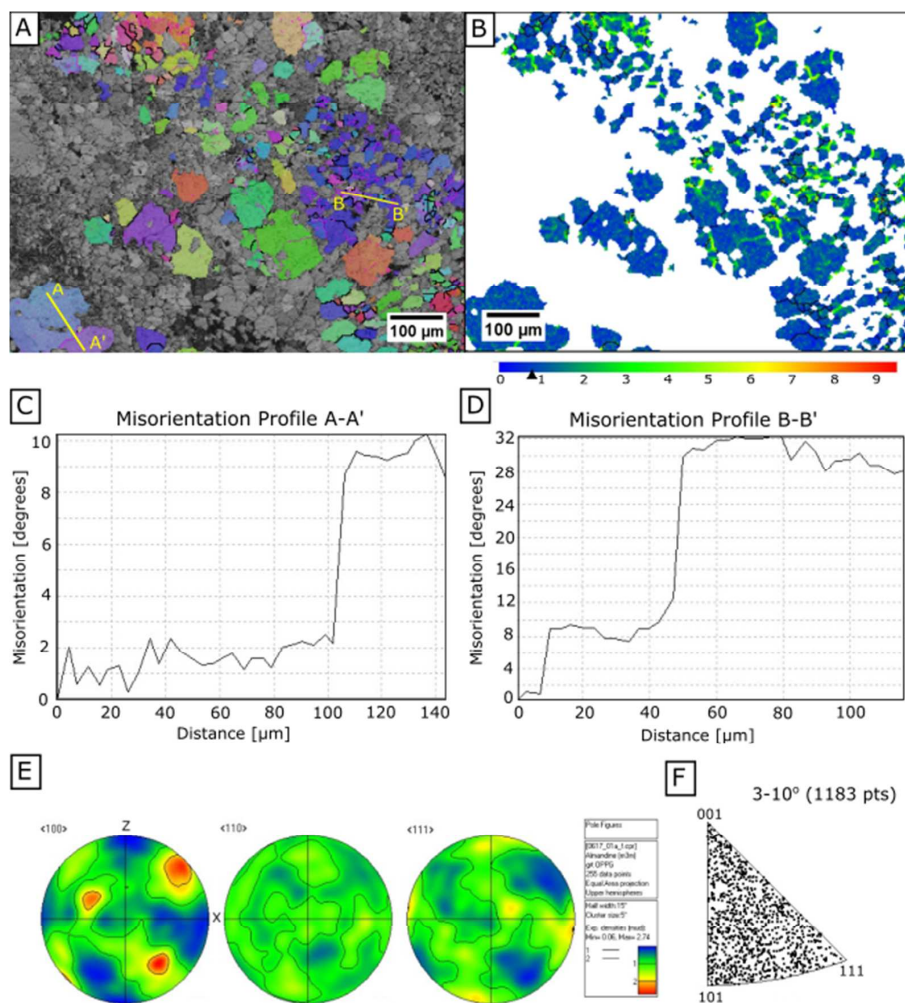

Fig. S3 EBSD results of low strain domain (sample 066B2). On EBSD-derived maps, high-angle boundaries (grain boundaries, misorientation > 10°) and low-angle boundaries (subgrain boundaries, misorientation > 3° and < 10°) were indicated with black and fuchsia lines, respectively. A) Phase map: Olivine (yellow), Plagioclase (white), Orthopyroxene (blue), Garnet (red), Hornblende (green). Red lines represent twinning boundaries in plagioclase. B) Inverse Pole Figure of Garnet in relation to the stretching lineation in the shear zone. Legend on bottom left corner. C) Local Misorientation Map, and legend, representing local misorientations from 0 (blue) to 9 degrees misorientation (red). The arrow indicates the average local internal misorientation. D) Misorientation profile A-A', location shown in figure C.
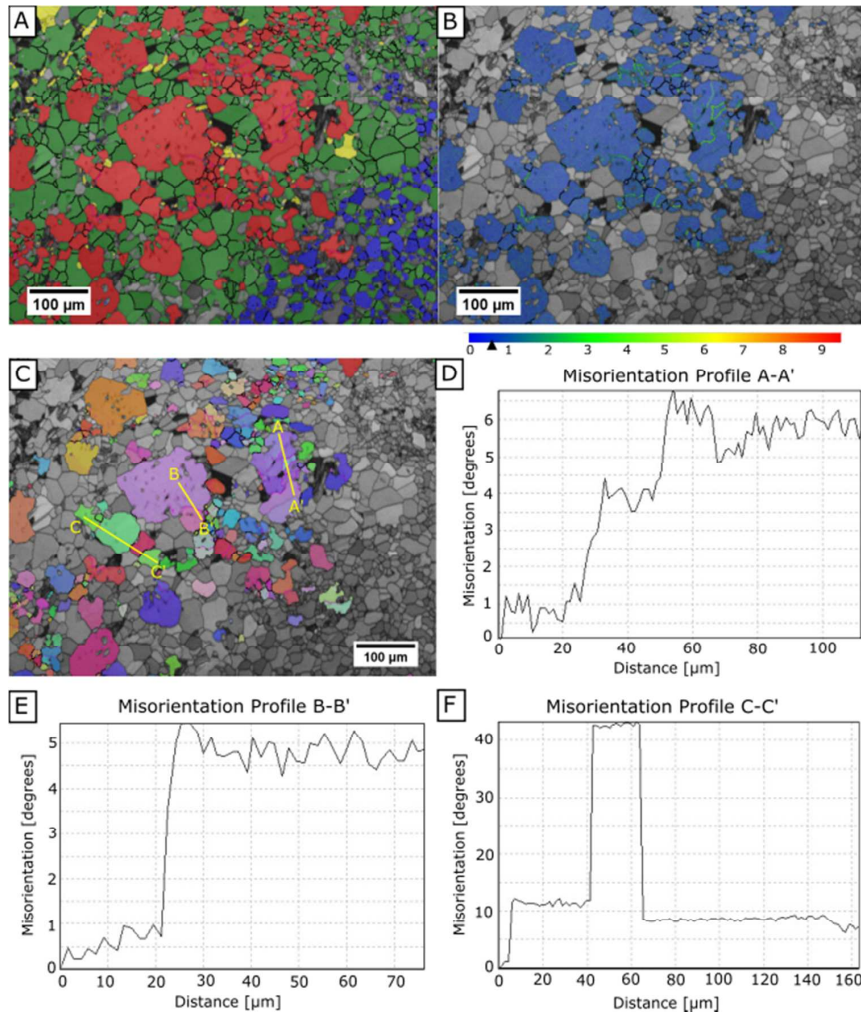
8

Fig. S4

Fig. S4 EBSD results of low strain domain (sample 066B2). E) Pole figures of Garnet. F) Pole Figure of Hornblende. G) Misorientation axis in crystal coordinates for low angle boundaries (3-10°).

Fig. S5

Fig. S5 EBSD results of intermediate strain domain (sample 0617). A) Inverse Pole Figure of Garnet. Legend as in Fig. S3B. B) Local Misorientation Map, and legend representing local misorientations from 0 (blue) to 9 degrees misorientation (red). The arrow indicates the average local internal misorientation. C) Misorientation profile A-A', location is shown in figure A. D) Misorientation profile B-B', location shown in figure A. E) Pole figures of Garnet. The trace of the shear foliation is oriented NW-SE, pole figures are oriented with the trace of the mylonitic foliation parallel to the diameter (E-W). F) Misorientation axis of low angle boundaries (3-10°) in crystal coordinates.

Fig. S6

Fig. S6 EBSD results of high strain domain (sample 0618). A) Phase map: Grt (red), Am (green), Opx (blue), Bt (yellow). B) Local Misorientation Map, and legend representing local misorientations from 0 (blue) to 9 degrees misorientation (red). The arrow indicates the average local internal misorientation. C) Inverse Pole Figure of Garnet. Legend as in Fig. S3B. D) Misorientation profile A-A', location is shown in figure C. E) Misorientation profile B-B', location shown in figure C. F) Misorientation profile C-C', location shown in figure C.

Fig. S7

11

Fig. S7 EBSD results of high strain domain (sample 0618). A) Pole figures of Garnet. The trace of the shear foliation is oriented NNE-SSW, pole figures are oriented with the trace of the mylonitic foliation parallel to the diameter (E-W). B) Pole figures of Hornblende. C) Misorientation axis of low angle boundaries (3-10°) in crystal coordinates.

Fig. S8

12

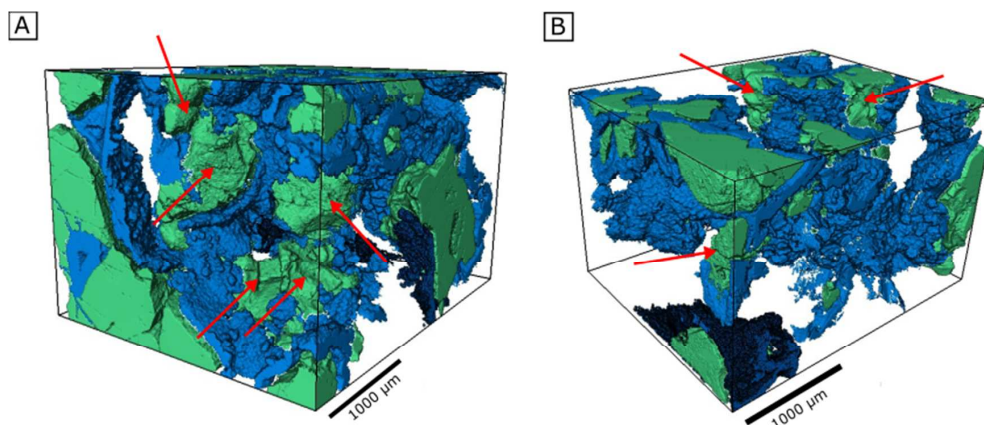**Fig. S8** The image shows the results of Statistical Region Merging technique for increasing Q. Scale as in image A. A) Original data. B) SRM Q=2. C) SRM Q=10. D) SRM Q=25: note that the image is more detailed. E, F, G) Histograms relative to the three different SRM parameters: note the increasing vertical lines for increasing Q.

Fig. S9

Fig. S9 Outputs of segmentation for olivine (green) and garnet (blue) grains, in the low strain domain (different viewing angles). The red arrows indicate olivine grains that are not completely enclosed by garnet coronas.

Fig. S10

Fig. S10 Label analysis of intermediate strain domain after erosion. The large interconnected voxel cluster is now divided in disconnected subvoxel clusters. Long side 2630 μm.

13
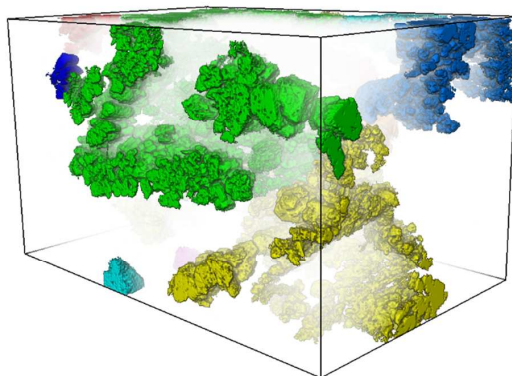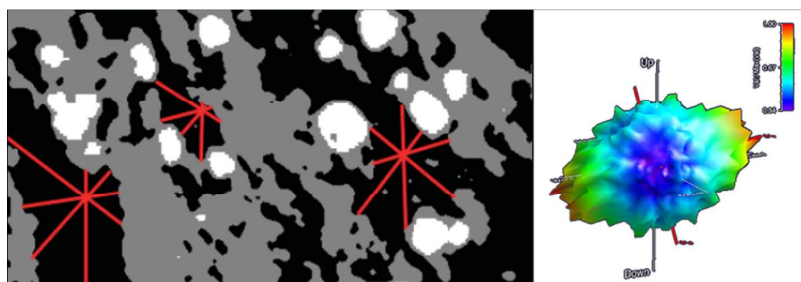
Fig. S11

Fig. S11 The tomographic data are first segmented to extrapolate the material of interest. Star points are placed within the segmented material: the distance of each star points to the next material boundary are calculated in many orientations and normalised. Simplified from Ketcham (2005).

Fig. S12

Fig. S12 Results of Quant3D analysis on eroded data, from low strain (A) to high strain (C). With increasing deformation, garnet grains evolve from isodiametric shapes to more progressively discoid shapes as a results of the deformation.

14
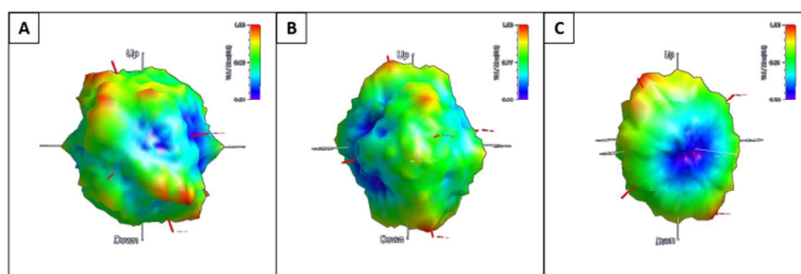
Sample	Na$_2$O	MgO	Al$_2$O$_3$	FeO	CaO	SiO$_2$	K$_2$O	TiO$_2$	Cr$_2$O$_3$	MnO	NiO	Total
#0618	0.009	6.853	21.605	28.263	5.709	38.981	0.004	0.039	0.004	0.705	0.000	102.171
#0618	0.036	6.405	21.874	28.018	5.360	39.270	0.003	0.097	-0.011	0.831	-0.011	101.873
#066B2	0.020	6.602	22.120	27.765	5.651	38.714	0.147	0.008	-0.003	1.157	0.015	102.196
#066B2	0.627	5.039	21.453	21.712	11.288	40.526	0.009	0.042	0.003	0.441	-0.008	101.131
#0617	-0.003	5.760	22.149	26.420	7.838	38.513	0.018	0.044	-0.009	0.865	-0.008	101.586
#0617	0.035	7.050	22.245	26.945	5.648	38.935	0.005	0.009	0.006	0.811	-0.010	101.679
#0617	0.044	5.801	22.150	25.930	8.612	38.965	0.006	0.051	-0.007	0.580	-0.009	102.122
#0617	0.021	5.868	22.291	25.077	9.592	38.815	0.000	0.065	-0.009	0.414	-0.013	102.120
#0617	0.030	6.173	22.366	24.130	9.262	38.685	0.001	0.043	0.004	0.971	0.005	101.668

Table S1 Electron microprobe chemical compositions of oxides in garnets, used to calculate the x-ray absorption coefficients.

	Low strain		Intermediate strain		High strain	
SiO2	38.86	39.17	38.33	38.06	38.9	38.56
TiO2	0	0.02	0	0	0	0
Al2O3	21.77	21.1	21.09	21.54	21.22	21.05
Cr2O3	0	0.01	0.01	0	0	0.03
Fe2O3	0.53	0.23	0.42	1	0	0.07
FeO	24.9	24.33	25.2	23.21	26.04	26.73
MnO	1.15	1.17	0.58	0.6	0.56	0.59
MgO	5.79	6.64	6.03	6.66	7.74	7.08
CaO	7.87	7.42	7.26	7.67	4.58	4.81
Na2O	0	0	0	0	0	0
K2O	0	0	0	0	0	0
Totals	100.86	100.1	98.92	98.74	99.04	98.92
Oxygens	12	12	12	12	12	12
Si	2.996	3.03	3.011	2.977	3.031	3.024
Ti	0	0.001	0	0	0	0
Al	1.978	1.924	1.953	1.986	1.949	1.946
Cr	0	0.001	0.001	0	0	0.002
Fe3	0.03	0.013	0.025	0.059	0	0.004
Fe2	1.605	1.574	1.655	1.518	1.697	1.753
Mn	0.075	0.076	0.039	0.04	0.037	0.039
Mg	0.665	0.765	0.706	0.776	0.899	0.827
Ca	0.65	0.615	0.611	0.643	0.382	0.404
Na	0	0	0	0	0	0
K	0	0	0	0	0	0
Sum	8	8	8	8	7.995	8

Table S2 Representative garnet structural formulae for the low (#066B2) and high (#0618) strain domain obtained from the microprobe analyses at the University of Münster.

15

Bins [µm³]	Low Strain	Cum. Freq.	Intermediate Strain	Cum. Freq.	High Strain	Cum. Freq.
2.00E+00	0		0		0	
4.00E+00	0		0		0	
8.00E+00	0		0		0	
1.60E+01	0		0		0	
3.20E+01	0		0		0	
6.40E+01	0		0		0	
1.28E+02	0		0		0	
2.56E+02	0		0		0	
5.12E+02	215	0.02%	2341	0.14%	3244	0.00%
1.02E+03	209	0.05%	5868	0.64%	2502	0.18%
2.05E+03	152	0.09%	2208	1.01%	1352	0.43%
4.10E+03	122	0.17%	822	1.29%	761	0.70%
8.19E+03	92	0.28%	348	1.54%	443	1.01%
1.64E+04	116	0.56%	174	1.78%	298	1.36%
3.28E+04	68	0.89%	97	2.04%	198	1.84%
6.55E+04	51	1.40%	62	2.40%	173	2.48%
1.31E+05	41	2.19%	42	2.85%	104	3.59%
2.62E+05	20	2.93%	33	3.59%	86	4.95%
5.24E+05	14	4.07%	26	4.74%	51	7.21%
1.05E+06	8	5.34%	14	6.03%	35	9.97%
2.10E+06	4	6.28%	17	9.24%	19	13.44%
4.19E+06	0	6.28%	8	11.80%	12	17.25%
8.39E+06	1	7.77%	3	13.94%	6	22.76%
1.68E+07	1	10.41%	4	19.72%	5	27.58%
3.36E+07	1	16.82%	0	19.72%	3	36.93%
6.71E+07	0	16.82%	0	19.72%	2	46.25%
1.34E+08	0	16.82%	0	19.72%	2	58.37%
2.68E+08	0	16.82%	0	19.72%	1	80.30%
5.37E+08	1	99.98%	0	19.72%	1	100.00%
1.07E+09	0	99.98%	1	100.00%	0	100.00%
Tot. Grt Vol.	**4.81E+08**		**8.19E+08**		**1.43E+09**	

Table S3 Frequency distribution data for non-eroded data. The first column of each dataset refers to absolute frequency, the second one to the cumulative frequency relative to the total amount of garnet in each sample.

16

Bins [µm³]	Low Strain (eroded)	Cum. Freq.	Intermediate Strain (eroded)	Cum. Freq.	High Strain (eroded)	Cum. Freq.
2.00E+00	0		0		0	
4.00E+00	0		0		0	
8.00E+00	0		0		0	
1.60E+01	0		0		0	
3.20E+01	0		0		0	
6.40E+01	0		0		0	
1.28E+02	0		0		0	
2.56E+02	0		0		2379	0.08%
5.12E+02	1101	0.14%	2428	0.15%	1628	0.18%
1.02E+03	638	0.30%	1215	0.15%	1183	0.34%
2.05E+03	390	0.49%	546	0.13%	827	0.55%
4.10E+03	208	0.70%	297	0.15%	604	0.86%
8.19E+03	153	1.00%	153	0.15%	361	1.23%
1.64E+04	102	1.40%	80	0.16%	281	1.82%
3.28E+04	61	1.91%	71	0.29%	213	2.72%
6.55E+04	49	2.69%	56	0.44%	156	4.00%
1.31E+05	45	4.22%	39	0.63%	126	6.10%
2.62E+05	18	5.37%	30	0.96%	87	8.82%
5.24E+05	15	7.14%	23	1.39%	70	13.57%
1.05E+06	5	8.78%	22	2.81%	35	18.14%
2.10E+06	2	9.85%	18	4.46%	25	24.47%
4.19E+06	4	14.19%	7	3.28%	18	34.18%
8.39E+06	1	16.95%	5	5.27%	8	42.66%
1.68E+07	0	16.95%	2	3.43%	6	55.06%
3.36E+07	1	22.88%	0	0.00%	4	73.84%
6.71E+07	1	37.39%	1	6.32%	3	99.83%
1.34E+08	2	99.86%	1	14.54%	0	99.83%
2.68E+08	0	99.86%	0	0.00%	0	99.83%
5.37E+08	0	99.86%	1	54.73%	0	99.83%
1.07E+09	0	99.86%	0	0.00%	0	99.83%
Tot. Grt Vol.	2.89E+08		5.83E+08		1.13E+09	

Table S4 Frequency distribution data for eroded data. Bins refer to cubic micrometres. The first column of each dataset refers to absolute frequency, the second one to the cumulative frequency relative to the total amount of garnet in each sample.

17

REFERENCES

Baker, D. R., Mancini, L., Polacci, M., Higgins, M. D., Gualda, G. A. R., Hill, R. J. & Rivers, M., 2012. An introduction to the application of X-ray microtomography to the three-dimensional study of igneous rocks. *Lithos*, **148**, 262–276

Denison, C. & Carlson, W. D., 1997. Three-dimensional quantitative textural analysis of metamorphic rocks using high-resolution computed X-ray tomography : Part II. Application to natural samples. *Journal of Metamorphic Geology*, **15**, 45–57.

Fusseis, F., Xiao, X., Schrank, C. & De Carlo, F., 2014. A brief guide to synchrotron radiation-based microtomography in (structural) geology and rock mechanics. *Journal of Structural Geology*, **65**, 1–16.

Goergen, E. T. & Whitney, D. L., 2012. Corona networks as three-dimensional records of transport scale and pathways during metamorphism. *Geology*, **40**, 183–186.

Gualda, G. A. R. & Rivers, M., 2006. Quantitative 3D petrography using x-ray tomography: Application to Bishop Tuff pumice clasts. *Journal of Volcanology and Geothermal Research*, **154**, 48–62.

Ketcham, R. A., 2005. Three-dimensional grain fabric measurements using high-resolution X-ray computed tomography. *Journal of Structural Geology*, **27**, 1217–1228.

Ketcham, R. A. & Ryan, T. M., 2004. Quantification and visualization of anisotropy in trabecular bone. *Journal of microscopy*, **213**, 158–71.

Nock, R. & Nielsen, F., 2004. Statistical Region Merging. *IEEE transactions on Pattern Analysis and Machine Intelligence*, **26**, 1452–1458.

Sayab, M., Suuronen, J., Holtta, P., Aerden, D., Lahtinen, R. & Kallonen, A. P., 2014. High-resolution X-ray computed microtomography: A holistic approach to metamorphic fabric analyses. *Geology*, **43**, 55–58.

Wang, W., Kravchenko, A. N., Smucker, A. J. M. & Rivers, M., 2011. Comparison of image segmentation methods in simulated 2D and 3D microtomographic images of soil aggregates. *Geoderma*, **162**, 231–241.

Whitney, D. L., Goergen, E. T., Ketcham, R. A. & Kunze, K., 2008. Formation of garnet polycrystals during metamorphic crystallization. *Journal of Metamorphic Geology*, **26**, 365–383.

18